Development of a Diver-Deployed Instrument for the Measurement of Sediment Density Gradients by X-Ray Attenuation Measurements

by

Matthew David Guild, B.S.

Thesis

Presented to the Faculty of the Graduate School of

The University of Texas at Austin

in Partial Fulfillment

of the Requirements

for the Degree of

Master of Science in Engineering

The University of Texas at Austin

August 2009

Development of a Diver-Deployed Instrument for the Measurement of Sediment Density Gradients by X-Ray Attenuation Measurements

Approved by
Supervising Committee:

Marcia J. Isakson

Preston S. Wilson

To Melissa

Development of a Diver-Deployed Instrument for the Measurement of Sediment Density Gradients by X-Ray Attenuation Measurements

Matthew David Guild, MSE
The University of Texas at Austin, 2009

Supervisors: Marcia J. Isakson
Preston S. Wilson

Acoustical interactions with ocean sediments effect a wide range of sonar applications in littoral environments. An important factor in understanding the acoustical behavior of the ocean bottom is how the sediment density changes with depth. Although there are existing techniques for obtaining information about sediment gradients, these methods are unable to provide direct measurements of the sediment density gradient without significantly disrupting the test site and requiring significant diver support for installation and implementation.

The proposed X-Ray Attenuation Measurement (XRAM) device aims to improve upon these existing techniques with the goal of being a portable diver operated device that can perform direct *in situ* measurements of sediment density gradients without significant disruption of the ocean bottom. To accomplish this, the XRAM utilizes the attenuation of x-rays passing through the sediment to measure the density as a function of depth, and is arranged in a compact, portable design that can be deployed and operated by a single diver. The layout and basic design of the XRAM device is discussed, and a physical model of its operation is developed. Results of experimental testing on homogeneous liquid samples and liquid/solid mixtures to evaluate the effectiveness of the XRAM device in measuring density gradients are presented. Based on the analysis of these results, recommendations of improved performance for future development are given.

Contents

List of Tables

List of Figures

Chapter 1

Introduction

1.1 Motivation for Seabed Density Gradient Measurements

Understanding acoustical interactions with ocean sediments is an important issue affecting underwater applications in littoral environments, such as long range sonar and identification of buried objects [1]. When the frequencies of interest are much larger than the grain size, the granular ocean bottoms can be approximated as a depth dependent effective fluid, described by the effective density and complex sound speed, as shown in Figure 1.1. In the figure, each layer is described by a density ρ, sound speed c, and thickness h. In the top half-space (representing the water column), an incident plane wave of pressure p_i is incident upon the sediment surface at an angle θ_0, which is then reflected as a plane wave of pressure p_r. The change in amplitude and phase of the reflected sound due to the effects of the sediment layers is described by the ratio of p_r to p_i, which is known as the reflection coefficient R and can be expressed as [2]:

$$R = \frac{R_{01} + \bar{R} e^{2jk_1 h_1 \cos\theta_1}}{1 + R_{01} \bar{R} e^{2jk_1 h_1 \cos\theta_1}}, \tag{1.1}$$

where $\bar{R}$ is the reflection coefficient at the interface between *medium 1* and *medium 2*, R_{01} is the reflection coefficient for a wave incident upon a half-space of density ρ_1 and sound speed c_1, given by

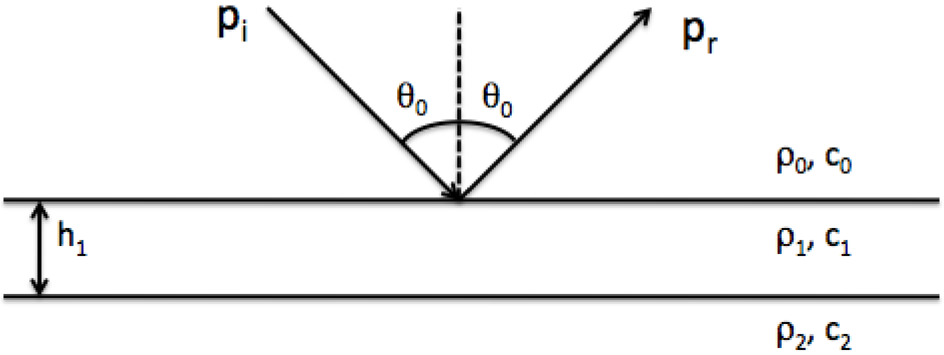

Figure 1.1: Illustration of a plane wave in a fluid half-space of density ρ_0 and sound speed c_0 incident on a horizontally stratified medium representing a simple model of the depth dependent behavior of the ocean bottom.

$$R_{01} = \frac{\rho_1 c_1 \cos\theta_0 - \rho_0 c_0 \cos\theta_1}{\rho_1 c_1 \cos\theta_0 + \rho_0 c_0 \cos\theta_1}, \tag{1.2}$$

and θ_1 is the incidence angle in *medium 1*, which is related to θ_0 by Snell's Law. In the case where *medium 2* is a half-space, $\bar{R}$ reduces to

$$\bar{R} = R_{12} = \frac{\rho_2 c_2 \cos\theta_1 - \rho_1 c_1 \cos\theta_2}{\rho_2 c_2 \cos\theta_1 + \rho_1 c_1 \cos\theta_2}. \tag{1.3}$$

Looking at the form of Equations (1.1) and (1.2), it can be seen that the changes in density significantly affect the amplitude and phase of the reflection coefficient, and how the density changes with depth (referred to as the density gradient) is an important factor in the observed reflection coefficient. The effect of the density gradient can be quite significant especially at higher frequencies, and differences up to 12 dB in reflection coefficient amplitude at 150 kHz were observed between an exponential and uniform density gradients [3]. Even at lower frequencies used for longer range sonar, a few decibels reduction in amplitude at the sediment interface can be significant since the sound may reflect off the ocean bottom multiple times.

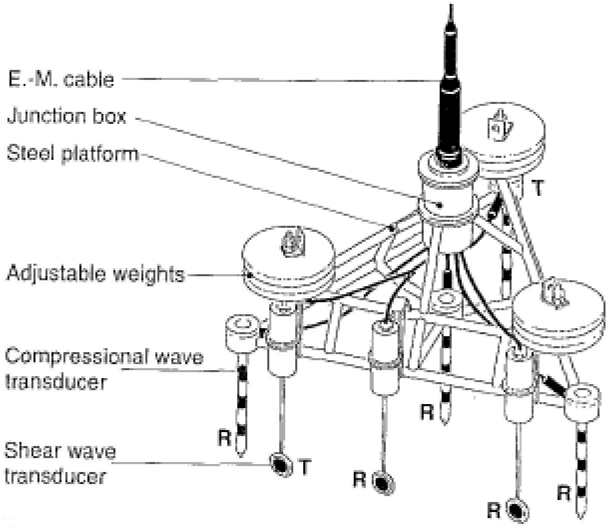

Figure 1.2: Layout of the ISSAMS, which operates by measuring sound speed and attenuation from differences in time and amplitude between acoustic transmitters (T) and receivers (R).

1.2 Existing Techniques for Measuring Sediment Gradients

Several techniques currently exist to determine ocean sediment grain properties and density gradients. The standard method which has been utilized for several decades is the analysis of core samples extracted from the ocean bottom. Core samples are obtained by inserting a long cylindrical tube with open ends into the sediment, which are then capped and brought to the surface, where they are either analyzed onboard the research vessel, or shipped to a land-based laboratory. To minimize disruptions to the sediment layering during transport to the surface and the subsequent analysis, the core sample is kept in an upright position throughout the entire process.

Once in a laboratory, several tests can be performed on the core sample to obtain relevant information about the sediment sound speed, porosity, grain density and grain size distribution as a function of depth. The sound speed is determined by time-of-flight measurements through the core sample and core liner at incremental

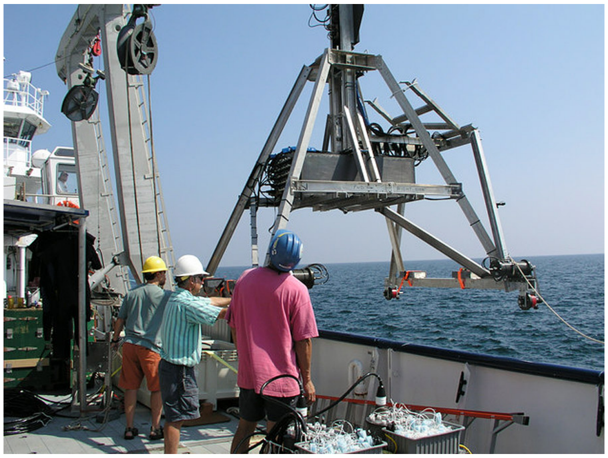

Figure 1.3: Deployment of the IMP system at SAX04 by APL:UW.

depths [4], after which thin layers of sediment are incrementally extruded out to perform the remaining analysis. Each thin sample is weighed, dried, and then weighed again to determine the porosity of the given sample layer. Grain size distribution can be determined by sifting and the average grain density can be obtained using a pycnometer [5]. Alternatively, x-rays can be used to obtain the sediment wet bulk density in a nondestructive manner using either x-ray computed tomography (CT) or the Gamma Ray Attenuation Porosity Evaluator (GRAPE) system [6].

For *in situ* sediment gradient measurements, one device that has been used is the In-Situ Sediment Acoustic Measurement System (ISSAMS), illustrated in Figure 1.2. This system is placed on the ocean bottom with the aid of divers, and a set of probes (each containing an acoustic transducer) are lowered into the sediment to a given depth. Compressional and shear wave properties of the sediment can be obtained using a time-of-flight measurement to determine sound speed and attenuation with a pulsed sine wave. However, compressional wave measurements are obtained using standard piezoelectric expander elements at 58 kHz, whereas the shear wave measurements are obtained using bimorph bender elements over the range of 100–1000 Hz [7].

A more recent device developed for obtaining sediment gradient measurements is the *In situ* Measurement of Porosity (IMP) system. This system utilizes

16 constant current probes arranged in a linear array with 1.0 cm spacing to obtain the conductivity as a function of depth. The IMP system has vertical and horizontal drivers, allowing it to obtain a 3-D map of sediment conductivity, which is then related to the sediment porosity by an empirical relation known as Archie's law [5]. Figure 1.3 shows the IMP system being deployed at the Sediment Acoustics Experiment 2004 (SAX04) by the Applied Physics Laboratory of the University of Washington (APL:UW) [8].

1.3 Motivation and Objectives for XRAM Device

Although each technique described above provides useful information about sediment gradients, these methods also have significant drawbacks. Core samples, which can provide a wealth of information about the granular composition of the sediment in addition to density gradients, are not performed *in situ* and can significantly disrupt the site under investigation. *In situ* measurements made by the ISSAMS can reveal valuable information about the compressional and shear speed gradient in a sediment sample, but does not reveal anything about the density or porosity profile. The IMP system, on the other hand, does provide *in situ* porosity information; however, it does not directly measure porosity or density, but infers these values from empirical relations based on conductivity measurements. In addition, the IMP is a relatively large system which requires significant diver support for deployment (shown in Figure 1.3) and significantly disrupts the test site.

The proposed XRAM device aims to improve upon these existing techniques with the goal of being a portable diver operated device that can perform direct *in situ* measurements of sediment density gradients without significant disruption of the test site. To accomplish this, the XRAM uses a similar technique to the GRAPE system or CT scans utilizing x-ray attenuation performed on core samples, but from a portable device that can operate in a littoral environment. The details of the XRAM device, relevant details on its operation, and the calibration and evaluation of measurement capabilities are described in the chapters that follow.

Chapter 2

Background

X-rays are a form of electromagnetic radiation with typical wavelengths in the range of 0.01 to 1 nm. However, the range of electromagnetic radiation for shorter wavelength (higher energy) x-rays can overlap with longer wavelength (lower energy) gamma-rays, and is typically distinguished by how the electromagnetic radiation is generated. X-rays are usually limited to radiation emitted from electrons, whereas radiation emitted from the nucleus is usually referred to as gamma-rays. X-rays with longer wavelengths are referred to in relative terms as "soft", and those with shorter wavelengths are referred to as "hard", which can be referenced to either the initial x-ray spectrum of interest or the general range of the x-ray spectrum.

2.1 X-ray Emission

X-rays are commonly produced by firing high energy electrons from a cathode of an evacuated chamber towards a target located at the anode, converting the kinetic energy of the electrons into x-rays, as illustrated in Figure 2.1. The kinetic energy can be converted either by a deflection of its path or a collision with an orbital electron of an atom in the target.

Bremsstrahlung, or "breaking radiation", occurs when high energy electrons interact with the electrical field of atomic nuclei in the target, as shown in the left panel of Figure 2.2. As the incident electron passes near the target nucleus, the positive charge of the nucleus decreases the momentum of the electron. This reduction in momentum of the incident electron leads to the emission of a photon.

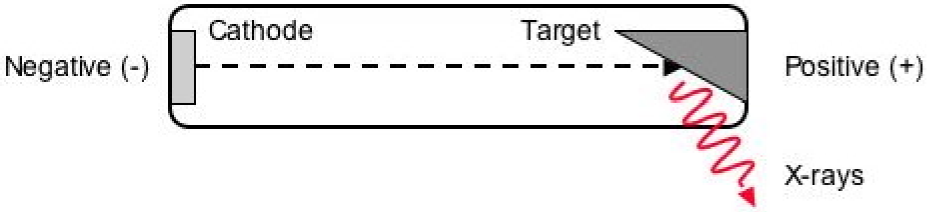

Figure 2.1: Schematic of an x-ray tube.

The amount of energy released is based on the position of the target nucleus and path of a given incident electron, producing a broad range of energy based on the probability of the interactions between the target atom and the incident electron, as illustrated in the right panel of Figure 2.2. The largest amount of energy released occurs when the incident electron transfers all of its momentum to emit a photon.

Another source of x-ray radiation occurs when a high energy electron interacts with an inner orbital electron in a target atom. If the incident electron has more energy than the binding energy of the orbital electron, then the collision will eject the orbital electron from the inner orbital of the target atom, leaving the target atom in an excited state. To return to its ground state, an electron from a higher

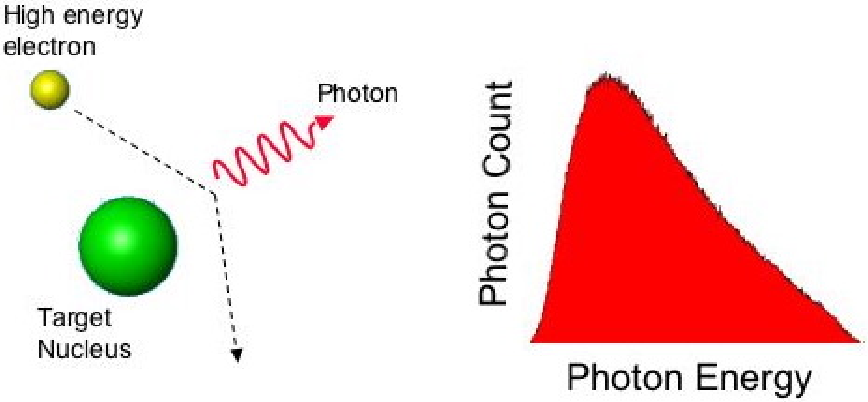

Figure 2.2: *Bremsstrahlung* X-ray emission by reduction in photon momentum (left), and corresponding x-ray energy spectrum (right).

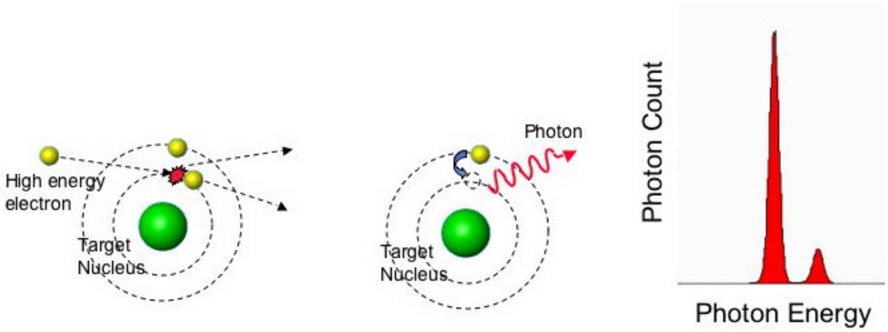

Figure 2.3: The process of characteristic x-ray emission. A high energy incident electron collides with inner orbital electron, ejecting the orbital electron (left), followed by an orbital electron from an outer shell filling the vacancy, releasing a characteristic x-ray (center) with the corresponding energy spectrum (right).

orbital can fill the lower vacancy, releasing a photon with a discrete energy equal to the difference in binding energies of the initial and final states of the electron. This process is illustrated in Figure 2.3. The photon emitted from this process is referred to as a characteristic x-ray, and the discrete amount of energy emitted is unique to each element. Alternatively, instead of emitting a characteristic x-ray, the target atom can return to its ground state by emitting an *Auger* electron. The probability of a characteristic x-ray being emitted is called the fluorescent yield [9].

Although the characteristic x-ray emissions are unique to each element, several different emissions can be expected for a given element, depending on which of 1,3,5, or 7 distinct energy levels in the K, L, M or N shells the initial and final states occur. To identify the x-ray characteristics, a common method is to use the letter of the shell in which the vacancy is being filled, and a Greek letter denoting the shell where the electron filling the vacancy originated. For example, an orbital electron from the L shell filling a vacancy in the K shell is often denoted as a K_α emission, and a transition from the M shell to the K shell is denoted as a K_β emission. For moderate to low atomic numbers, most characteristic x-ray emissions of interest involve vacancies in the K shell, the inner most electron shell.

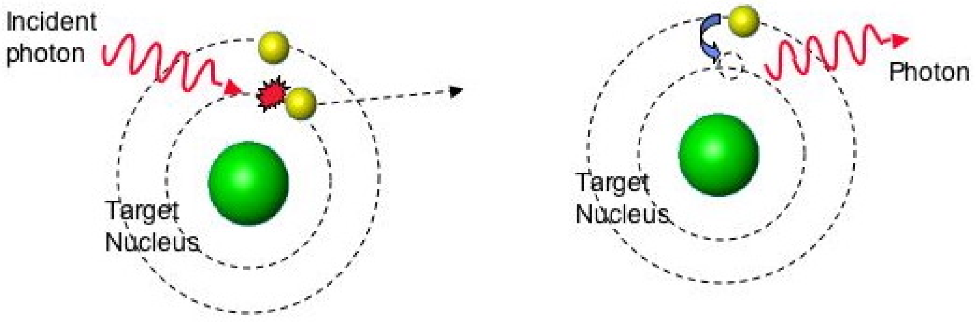

Figure 2.4: The process of photoelectric absorption. An incident photon is absorbed by an inner electron, ejecting the particle (left). A bound electron from a higher orbital drops to fill the vacancy, releasing a characteristic x-ray (right).

2.2 Interaction of X-rays

For x-rays in the energy range of interest for the XRAM device, the two main types of interactions that contribute to x-ray attenuation through a material are photoelectric absorption and Compton scattering. In photoelectric absorption, shown in Figure 2.4, an incident photon is absorbed by an inner orbital electron, which is then ejected. The ejected electron, called a photoelectron, is emitted with an energy equal to the incident photon minus the binding energy and ionizes the absorbing atom. The atom then returns to ground state by recapture of a free electron, ejection of an *Auger* electron or emission of a characteristic x-ray.

Compton scattering occurs when an incident photon collides with an orbital electron in an outer shell, which is referred to as the recoil electron. The collision transfers energy to the recoil electron and scatters the remaining energy at an angle relative to the incident photon, as illustrated in Figure 2.5. Since the binding energy of an outer shell electron is negligible compared to the incident photon, the decrease in energy in the scattered photon depends only on the angle. Although the energy of the scattered photon is independent of the atomic number, Z, of the absorbing atom, the probability of Compton scattering occurring is proportional to the number of outer shell electrons, and therefore is proportional to Z [9].

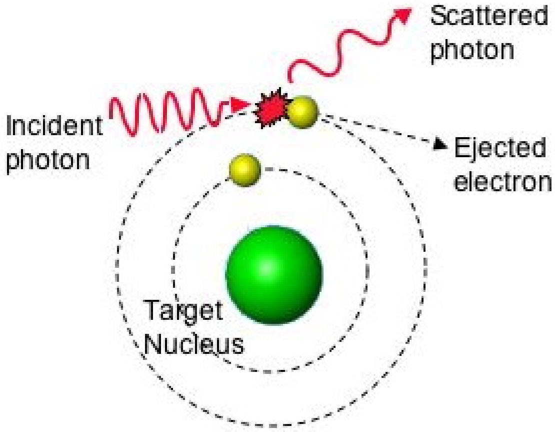

Figure 2.5: The Compton Effect.

2.3 Modeling X-ray Attenuation

The attenuation of x-ray intensity due to absorption through a material varies exponentially with the mass thickness of the absorbing material. The change in intensity can be written explicitly as

$$I = I_0 \, e^{-\frac{\mu}{\rho}\bar{x}}, \tag{2.1}$$

where I_0 is the initial intensity, μ is the linear attenuation coefficient, ρ is the density, and $\bar{x}$ is the mass thickness, given by the product of the density and the sample thickness. The expression given by Equation (2.1) assumes that the x-rays are perfectly collimated in a narrow beam and are monoenergetic. Under these conditions, the linear attenuation coefficient μ is a constant, but in general its value can vary significantly with energy and the atomic number of the attenuating material.

The ratio of the linear attenuation coefficient μ and the density ρ is known as the mass attenuation coefficient, and represents a normalized value for comparing the attenuation between two different materials. Mass attenuation coefficients for materials and energy ranges commonly encountered using the XRAM device are

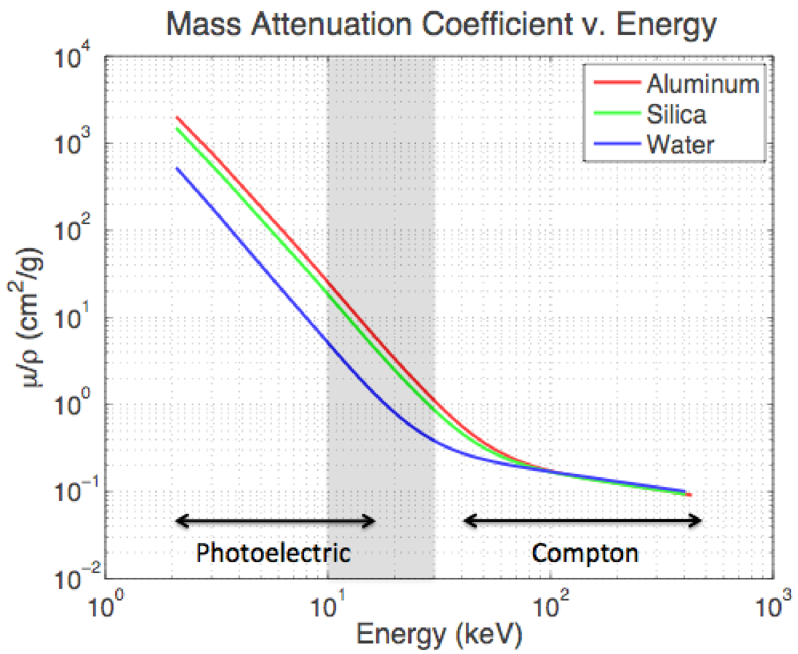

Figure 2.6: Mass attenuation coefficient for aluminum, silica and water over the photoelectric and Compton regions, with the range of interest for the XRAM device shown in gray [10].

shown in Figure 2.6. From the figure, it can be seen that the mass attenuation coefficient $\frac{\mu}{\rho}$ varies significantly with energy and atomic number. Also, the mass attenuation coefficient for a given material does not change with a physical change in state [9]. As a result, lower energy x-rays will attenuate more than higher energy x-rays, which leads to the hardening of an x-ray spectrum. The mass attenuation coefficient is a function of the absorbing material (described by the atomic number Z) in the region where photoelectric absorption dominates, but is relatively independent of atomic number in the Compton region.

For compounds and mixtures, the mass attenuation coefficient can be determined by

$$\left(\frac{\mu}{\rho}\right)_{\text{comp}} = \sum_{n}^{N} w_n \left(\frac{\mu}{\rho}\right)_n, \tag{2.2}$$

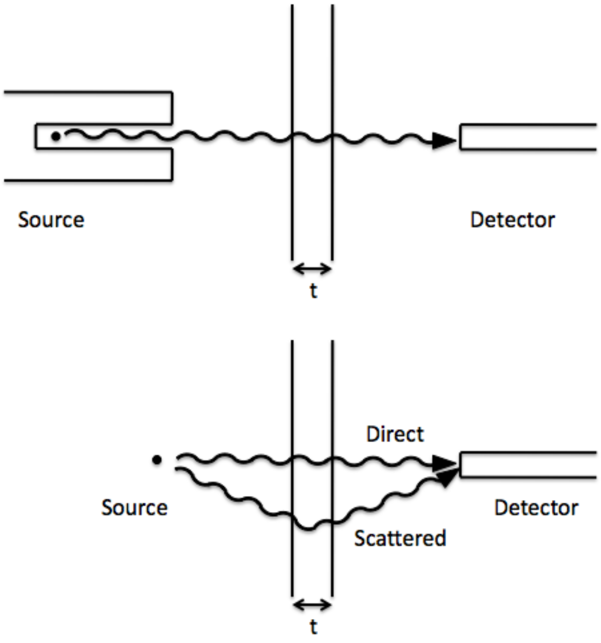

Figure 2.7: Measurement of x-ray attenuation using a narrow beam source (top) and a broad beam source (bottom).

where the compound or mixture mass attenuation coefficient, $\left(\frac{\mu}{\rho}\right)_{\text{comp}}$, is the average of N components by weight, with each component having a mass attenuation coefficient $\left(\frac{\mu}{\rho}\right)_n$ and weight fraction w_n, for $n = 1, 2, \ldots, N$.

For a source with a broad beam, such as the omnidirectional point source illustrated in the configuration shown in the bottom panel of Figure 2.7, Equation (2.1) can be modified to describe the intensity measured at the detector such that

$$I = \frac{1}{r^2} B(\frac{\mu}{\rho}\bar{x}, E) I_0 \, e^{-\frac{\mu}{\rho}\bar{x}}, \tag{2.3}$$

where the $\frac{1}{r^2}$ term accounts for spherical spreading and $B(\frac{\mu}{\rho}\bar{x}, E)$ is a multiplicative correction factor to account for the additional contribution from scattered x-rays called the *buildup factor*. Buildup factors have been investigated extensively for radiation shielding applications, and several useful approximate forms have been developed. One such approximation is obtained by expressing the buildup factor as a truncated Taylor series, written in general as

$$B(\frac{\mu}{\rho}\bar{x}, E) \approx \sum_{n=1}^{N} A_n(E) e^{-\alpha_n(E)\frac{\mu}{\rho}\bar{x}}, \tag{2.4}$$

where A_n and α_n are parameters fit to experimental data for a given material as a function of energy.

Approximate forms of the buildup factor, including the Taylor form, assume an omnidirectional monoenergetic point source radiating into an infinite medium. In most applications of interest for radiation shielding, the source and detector are in air (which is approximated as a vaccuum), separated by a shielding material of thickness t, as in the configurations shown in Figure 2.7. In this situation, approximate forms of the buildup factor are effective provided the sample thickness t is sufficiently thick. The relative thickness of the sample is based on the mean free path λ, which represents the average distance traveled by an x-ray between interactions within the material, and is given by $\lambda = \frac{1}{\mu}$ [11]. Therefore, the relative thickness can be expressed as

$$\frac{t}{\lambda} = \mu t = \frac{\mu}{\rho}\bar{x}. \tag{2.5}$$

By using only the leading order term in Equation (2.4), good agreement can be obtained for $\frac{\mu}{\rho}\bar{x} \gtrsim 3$ [11]. To obtain results for values below this relative thickness, the standard practice [ANSI/ANS-6.4.3-1991] is to keep two terms when using the Taylor form and to express $A_2(E)$ in terms of $A_1(E)$:

$$B(\frac{\mu}{\rho}\bar{x}, E) \approx A_1(E) e^{-\alpha_1(E)\frac{\mu}{\rho}\bar{x}} + (1 - A_1(E))\, e^{-\alpha_2(E)\frac{\mu}{\rho}\bar{x}}, \tag{2.6}$$

where the parameters A_1, α_1 and α_2 are given in Table 2.1 for some typical materials used in radiation shielding applications. These parameters are fit from experimental data, and even though the Taylor form of the buildup factor changes monotonically as illustrated in Figure 2.8, the individual parameters using the two term expansion do not.

In the arrangement shown in the bottom panel of Figure 2.7, the Taylor form given by Equation (2.6) was applied by assuming that the material surrounding the source and detector had a negligible effect on the scattering or attenuation of the

Energy (keV)	Air			Water		
	A_1	α_1	α_2	A_1	α_1	α_2
15	1.585	-0.0032	0.2387	1.675	-0.0030	0.2241
20	2.269	-0.0146	0.3247	2.473	-0.0143	0.2906
30	6.729	-0.0380	0.2191	7.524	-0.0406	0.1755
40	77.573	-0.0316	0.0001	83.292	-0.0382	-0.0066
50	179.362	-0.0624	-0.0374	98.191	-0.0801	-0.0282

Energy (keV)	Concrete			Lead		
	A_1	α_1	α_2	A_1	α_1	α_2
15	1.110	0.0000	0.1166	1.020	-0.0003	0.2000
20	1.192	-0.0010	0.2185	1.020	-0.0003	0.2000
30	1.505	-0.0072	0.3932	1.020	-0.0003	0.2000
40	2.440	-0.0131	0.3378	1.040	-0.0004	0.3000
50	3.846	-0.0241	0.2267	1.040	-0.0012	0.2500

Table 2.1: Taylor form buildup parameters for air, water, concrete, and lead.

x-ray intensity measured at the detector. To account for multiple layers, the Broder method can be used to approximate the total buildup factor as the sum of the first layer closest to the source plus marginal effects from each subsequent layer, which for a general N layer arrangement can be written as [11]

$$B_{\text{tot}} \approx \sum_{n=1}^{N} B_n \left(\sum_{i=1}^{n} t_i \right) - \sum_{n=2}^{N} B_n \left(\sum_{i=1}^{n-1} t_i \right), \tag{2.7}$$

where B_n and t_n are the buildup factor and thickness of the n^{th} layer, respectively.

The buildup factors discussed above are defined for normal incidence only, but in general, buildup factors need to be defined for each angle. To account for this, Equation (2.3) becomes

$$I = \frac{1}{r^2} B(\frac{\mu}{\rho}\bar{x}, \cos\theta, E) I_0 \, e^{-\frac{\mu}{\rho}\frac{\bar{x}}{\cos\theta}}, \tag{2.8}$$

for an incidence angle θ. However, this can be of limited practical value since the experimental data used to determine Taylor form parameters (or any other approximation technique) exist for only a few discrete angles. Instead, the buildup factor at a given angle can be approximated by

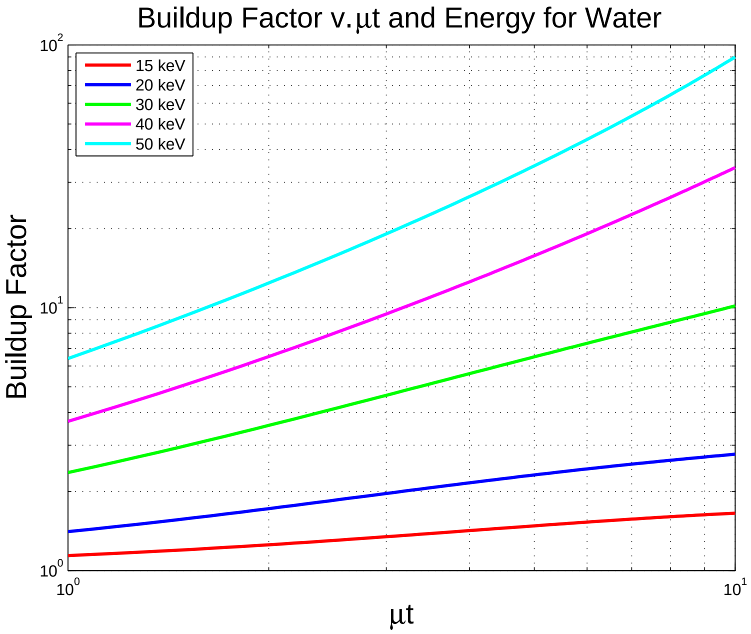

Figure 2.8: Taylor form approximation of the buildup factor as a function of μt and E for water.

$$B(\frac{\mu}{\rho}\bar{x}, \cos\theta, E) \approx B(\frac{\mu}{\rho}\frac{\bar{x}}{\cos\theta}, E), \tag{2.9}$$

where the right hand side is simply the normal incidence buildup factor, and can be approximated using the Taylor form given in Equation (2.6). Equations (2.6) and (2.9) will be used later in this work to relate the sample density gradient to the XRAM device measurements.

Chapter 3

XRAM Layout

3.1 Overview

The X-Ray Attenuation Measurement (XRAM) device is a diver deployable tool for use in analyzing *in situ* ocean sediment gradients by observing the change in x-ray attenuation over a given section of the sea bottom. The XRAM device, shown in Figure 3.1, is comprised of a cylindrical main body measuring 33.0 cm long and 25.4 cm in diameter, a 24.1 cm long probe sheath and a handle. The structure of the XRAM is constructed from anodized aluminum 6061 alloy, with a polycarbonate tubular window on the main body allowing visual inspection of the XRAM instrumentation, and a low density polyethylene (LDPE) x-ray window on the bottom of the main body. The XRAM device has a dry weight of 22.2 kg, providing a slight negative buoyancy in seawater even though the main body remains air filled while submerged.

Figure 3.2 shows an exploded view of the XRAM device, and highlights the major components of the instrument. These systems can be divided into two main groups: the x-ray system, which involves the generation and detection of x-rays, and the supporting systems, which includes data acquisition, power and control systems that enable the measurement collection and coordination of the x-ray system.

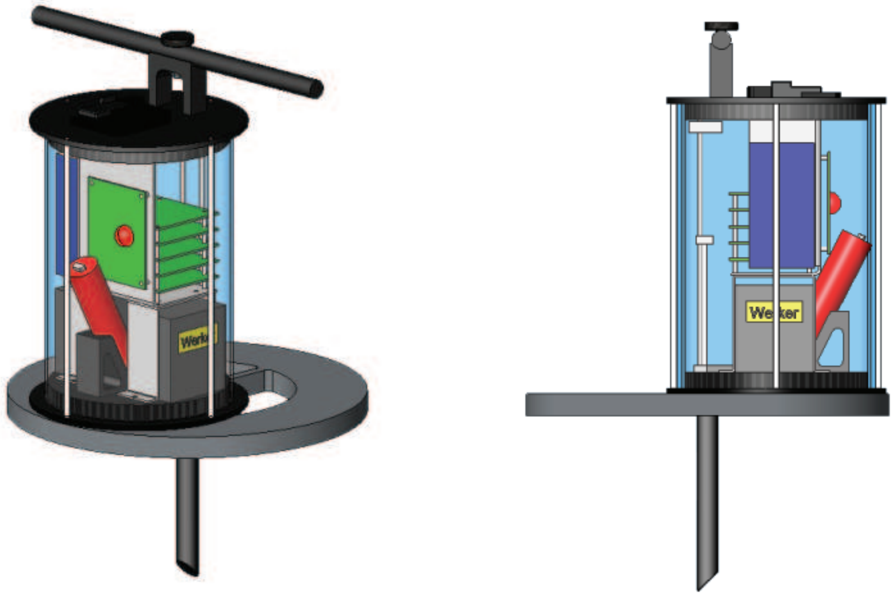

Figure 3.1: Two views of the XRAM device.

3.2 X-ray Systems

3.2.1 Source

The x-ray source used in the XRAM is a model Eclipse II Oxford Instruments cold cathode source that is capable of producing x-rays up to 30 keV, and is shown in Figures 3.1 and 3.2. This source is optimized for portability and remote operation, making it ideal for use in the XRAM device. Although limited to 30 keV, the cold cathode filament offers a more efficient method for providing the electrons at the cathode in terms of power consumption than a conventional heated filament. It should be noted that the term “cold” is relative to a conventional filament, and refers to operation at room temperature without any heating necessary. Heating the filament on a conventional source requires a separate power source, thus requiring too much power to be supplied by the XRAM batteries during diver deployment.

Additional features of the source are also beneficial for operation of the XRAM device. A wide angle x-ray cone (greater than 125°) can cover a large area, allowing the source to be fixed while the detector moves through the irradiated re-

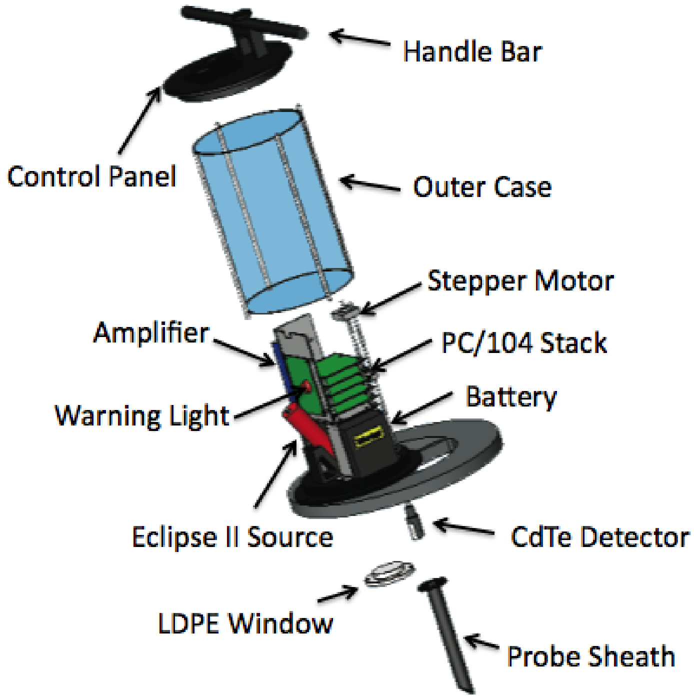

Figure 3.2: Exploded view highlighting all the major components of the XRAM device.

gion. For analysis of a wide range of mass thicknesses, the source has independent controls for x-ray energy and firing rate. For a given mass thickness and maximum energy, varying the firing rate allows for the depth range to be adjusted.

Due to the relatively low energies of the Eclipse II source compared to a heated filament, a silver target is used since it emits K_α and K_β characteristics allowing for spectral calibration. From Figure 3.3, it can be seen that the Eclipse II emits a broadband spectrum below 30 keV due to *bremsstrahlung* in addition to the K_α and K_β characteristics from the silver target. Although the energy range of the source can be adjusted, the XRAM is operated using the maximum x-ray energy range of 30 keV for optimal performance, based on the detector energy efficiency and the exponential increase in absorption with decreasing energy.

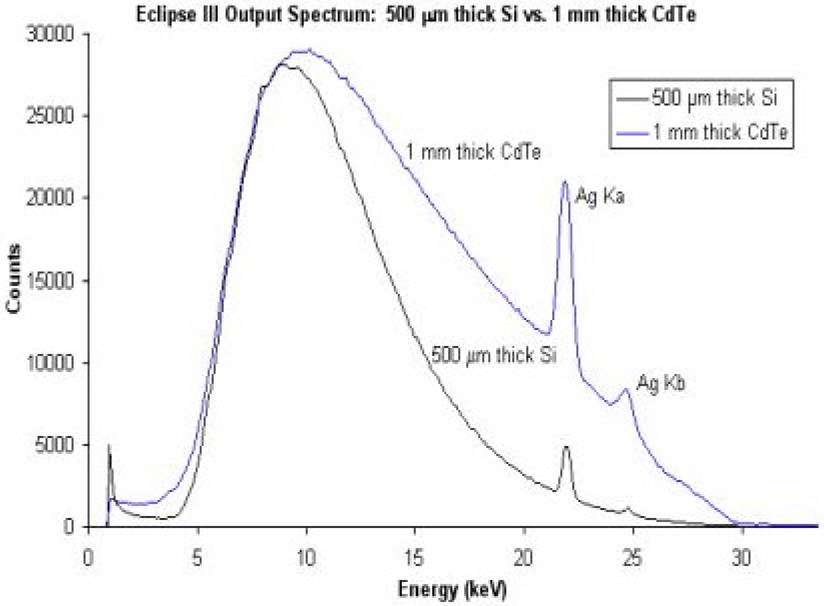

Figure 3.3: Eclipse II source spectrum measurements provided by the manufacturer using a silicon diode detector (black) and a CdTe detector (blue) (courtesy of Amptek, Inc.).

3.2.2 Detector

A key aspect of the x-ray detector on the XRAM device is its ability to detect changes in x-ray intensity, and the sensitivity with which it can perform this task. In addition to high sensitivity, other factors must be considered to meet the unique needs of the XRAM device, including small detector size, spectral efficiency and power consumption for the entire x-ray detection system. To meet these requirements, a custom designed 10 mm x 10 mm x 2 mm cadmium telluride (CdTe) crystal coated in electrically insulating epoxy was utilized (Figure 3.4). The CdTe crystal provides a voltage proportional to the total amount of energy incident on the face of the detector, and is connected to a small high gain amplifier to provide sufficient sensitivity. Thus, the detector does not give any spectral information about the incident x-rays or how the spectrum changes across the face of the detector, instead giving only a single measurement of the integrated response over energy and the

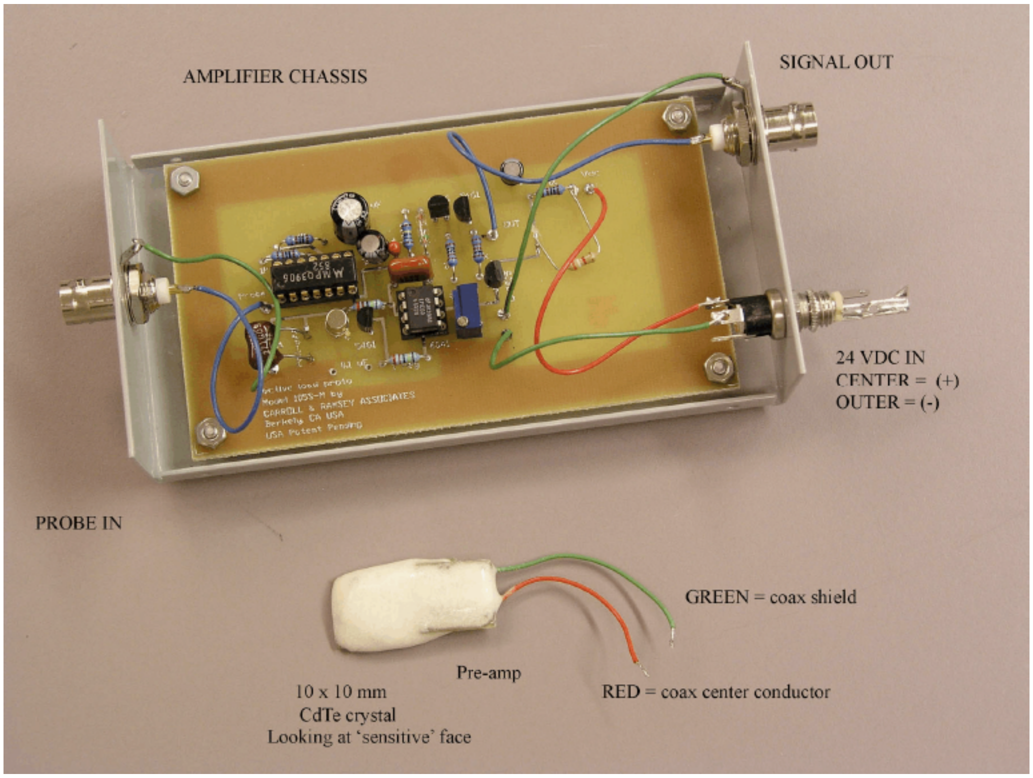

Figure 3.4: XRAM x-ray detection system: 10 mm x 10 mm x 2 mm epoxy coated CdTe detector model 105SM-X (bottom) and high gain amplifier chassis (top) (courtesy of Carroll & Ramsey Associates).

surface of the detector.

To relate the intensity at the detector surface with the voltage output, the detector sensitivity as a function of energy was needed, which is referred to as the detector efficiency. The detector efficiency can have a significant effect on the measured spectrum, as can be seen in Figure 3.3. In this figure, the same Eclipse II source spectrum is measured using two detectors with different efficiencies, resulting in noticeably different spectra. Figure 3.5 illustrates the detector efficiency of the CdTe detector used in the XRAM device. Although the detector does not have a flat response across all energies, it does detect x-rays from 14 keV through 80 keV.

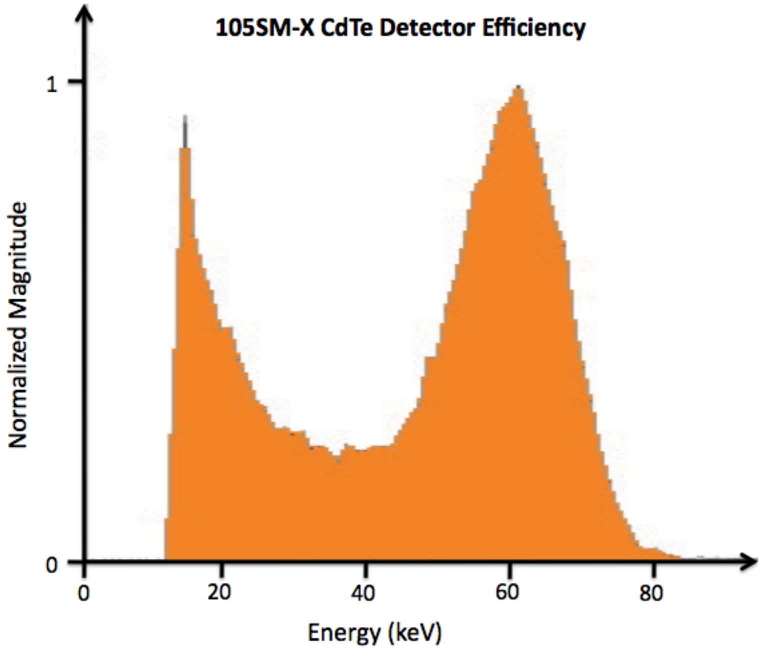

Figure 3.5: Normalized detector efficiency provided by the manufacturer for the model 105SM-X CdTe detector.

3.3 Supporting Systems

3.3.1 Power System

For portable deployment, the XRAM device must provide power for all the onboard systems without the assistance of any external power source. To accomplish this, two rechargeable batteries are utilized, each producing 12 V with a capacity of 5 amp-hours. As illustrated in Figure 3.2, the batteries are located at the bottom of the main body. Due to the operation of the XRAM device in relatively difficult conditions for electronic components such as exposure to salt water or impacts, an absorbed glass mat (AGM) lead-acid battery was used, which provides a rugged power source that is both spill-proof and impact resistant.

The two batteries provide DC power to all the systems on the XRAM device, including the cold cathode x-ray source. The Eclipse II source has two independent inputs– one for the voltage of the x-ray tube, which determines the total maximum

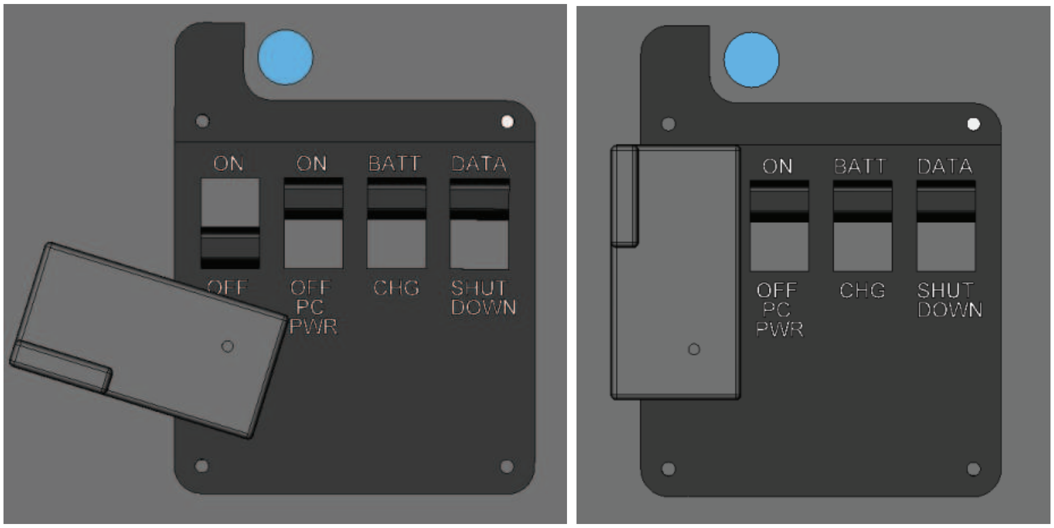

Figure 3.6: XRAM device control panel showing the x-ray toggle switch cover unlocked (left) and locked (right).

energy of the x-rays produced, and one for the current, which controls the electron firing rate and thus the x-ray intensity. To accomplish this, two potentiometers were used to allow independent control of each input to the x-ray source.

3.3.2 Data Acquisition System

To operate, measure and record the data obtained using the x-ray source and detector, a PC/104 embedded computer stack was used. This system operates just like a PC, and contains the modules for A/D conversion, data acquisition and a wireless network card. The data acquisition process was controlled using a LabView virtual instrumentation (VI) code stored in memory on the PC/104 stack, and can be executed by the operator using the “data” toggle switch on the control panel (illustrated in Figure 3.6). The voltage output from a predetermined number of detector locations is recorded and saved, which can be transferred by a wireless network connection to a laptop computer for analysis after returning to the surface.

3.3.3 Control System

To facilitate the data collection and operation using the embedded PC/104 stack, an interface to accept diver input was necessary. A control panel located near the handle is shown in Figure 3.6, which contains toggle switches to turn on the PC/104, engage the x-ray source and begin data collection. To ensure that the divers could move to a safe distance after the x-ray source is turned on, several safety features are incorporated into the control system. First, a 10 second delay from when the x-ray source toggle switch is engaged before the x-ray source turns on allows the diver time to swim to a safe distance (1 m) while the measurements are taken. Second, to notify all divers in the area that the x-ray source is on, a high intensity flashing light is emitted for the entire time the x-ray source is on. Finally, to prevent the x-ray source from accidental engagement, a cover which holds the x-ray source toggle switch in the off position is used during the transport of the XRAM device to and from its test site. The unlocked and locked positions of the x-ray source cover are illustrated in the left and right panels of Figure 3.6, respectively.

Chapter 4

Theory

The interaction of x-rays with a material was described in Chapter 2 in the context of atomic and subatomic particles and how x-ray attenuation varies with the properties of an absorbing material. For the applications of the XRAM device, the geometry of the source and detector with respect to a horizontally stratified sample must be considered. Based on this arrangement, a model relating the measured output of the detector to the physical properties of the sample being investigated can be determined. Using numerical techniques, the expressions developed for the XRAM model can be inverted to obtain the physical properties as a function of detector output.

4.1 Calculation of Mass Thickness

In Chapter 2, the attenuation of x-rays passing through a material was described using Equation (2.1), and was dependent only on the mass attenuation coefficient and the mass thickness of the sample. Unlike the mass attenuation coefficient discussed in Section 2.3, the mass thickness is independent of atomic structure and is determined by the product of the density and the thickness of the material. As a result, the geometry of the XRAM device will need to be accounted for at each position of the x-ray detector probe. The required analysis is performed in this section, for both the sample being investigated and the probe sheath.

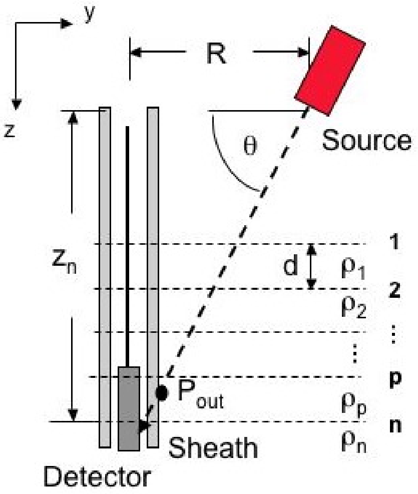

Figure 4.1: Illustration of XRAM geometry for a horizontally stratified sample.

4.1.1 Horizontally Stratified Media

Density gradients of particular interest to applications of the XRAM device are those involving water-saturated sediments, which in the ocean environment often exhibit horizontal stratification. Due to the discrete detector positions, the sample is modeled as having a discrete number of horizontally stratified layers of thickness d and constant density, as shown in Figure 4.1. The figure shows the detector at a fixed horizontal distance R from the source at depth z_n, and a sample with n stratified layers of densities $\rho_1, \rho_2, \ldots, \rho_n$, respectively.

The thickness of each layer, d, is determined by the detector step increment, since there cannot be more unknown densities than data points. The position of each layer is defined relative to the detector position, so that the n^{th} layer is centered at the n^{th} detector depth. Smaller step increments in the detector position improve the resolution of the density gradient, but result in several layers covering the detector face at any one time, as can be seen in Figure 4.1. In addition, the sample layers are separated from the detector by the probe sheath, so on any given path from the source to a point on the detector the maximum depth measured is actually at the

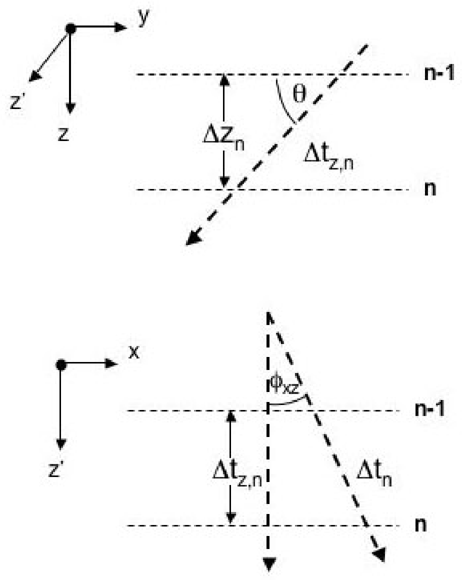

Figure 4.2: Mass thickness through an individual layer of a horizontally stratified sample.

depth of point P_{out}. As illustrated in the figure, this point can be in a different layer than that of the arrival point on the detector face, and is denoted as the p^{th} layer.

From Figure 4.1, it can be seen that for a horizontally stratified sample the total attenuation measured at a point on the detector face will be a combination of the attenuation from a series of layers. For each layer, the attenuation at a given energy is described by Equation (2.1), and is determined by the mass attenuation coefficient and the mass thickness of the layer. Although the mass attenuation coefficient only depends on the atomic composition of the layer, the mass thickness depends on the unknown density and the path length through each layer, which will be different for each point on the detector face for a given step due to the different angle between the source and detector.

From the geometry of the n^{th} layer in the y–z plane illustrated in Figure 4.2, the in-plane thickness $\Delta t_{z,n}$ can be calculated as a function of the depth into the layer, Δz_n. Due to the finite width of the detector, there will also be a change in thickness relative to the angle for out of plane motion (in or out of the page in

Figure 4.1). From the geometry of the x–z' plane (with the positive x-axis out of the page), the total path length through the n^{th} layer Δt_n can be related to $\Delta t_{z,n}$ by

$$\Delta t_n = \frac{\Delta t_{z,n}}{\cos \phi_{xz}}, \tag{4.1}$$

which is related to Δz_n by

$$\Delta t_{z,n} = \frac{\Delta z_n}{\sin \theta}. \tag{4.2}$$

To find the total mass thickness $\bar{x}$ at a given θ and ϕ_{xz}, a summation of the individual mass thicknesses of each of the N layers can be performed:

$$\bar{x} = \sum_{n=1}^{N} \rho_n \Delta t_n = \left(\frac{1}{\sin \theta \, \cos \phi_{xz}} \right) \sum_{n=1}^{N} \rho_n \Delta z_n. \tag{4.3}$$

As previously mentioned, the maximum depth measured in the sample occurs at the point P_{out} in the p^{th} layer shown in Figure 4.1, the depth of which can be denoted z_P. Since z_P will generally not coincide with the layer interfaces, the last layer will have a depth less than the single layer thickness, d, while all the layers above the p^{th} layer will have $\Delta z_n = d$. The resulting expression for Δz_n can be simply expressed as

$$\Delta z_n = \begin{cases} d, & n < p, \\ (z_P - z_{n-1}), & n = p. \end{cases} \tag{4.4}$$

4.1.2 Aluminum Probe Sheath

In a similar manner, an expression for the mass thickness of the aluminum probe sheath can be determined. Although the sheath is not part of the sample being investigated, it will attenuate the intensity of the incident x-rays, and needs to be accounted for. This is especially important since the attenuation resulting from the relatively thin probe sheath (compared to the sample thickness) can be significantly larger than that of a liquid or a saturated sediment of the same mass thickness, as highlighted by the mass attenuation coefficients given in Figure 2.6. Though the attenuation will be the same at a given depth for all tests performed by the

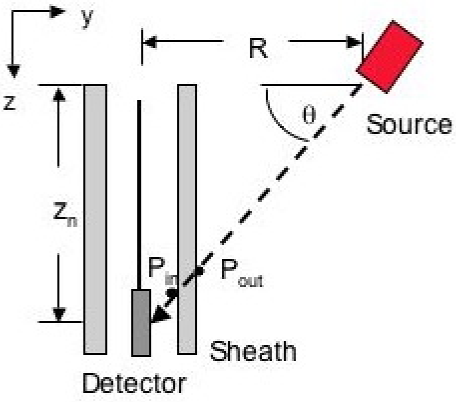

Figure 4.3: Mass thickness through sheath in y–z plane.

XRAM, it can not simply be calibrated or normalized out because of the nonlinear relationship between energy and spatial coordinates in the measured voltage, which is discussed in more detail in the next section.

Due to the potentially large influence of the sheath attenuation on the measured output, it is important to accurately account for the changes in thickness that occur at different relative angles between the source and detector. The mass thickness will simply be the product of the density of aluminum ρ_{Al}, and the path length through the sheath Δt_{Al}:

$$\bar{x}_{\mathrm{Al}} = \rho_{\mathrm{Al}} \Delta t_{\mathrm{Al}}. \tag{4.5}$$

From the geometry illustrated in Figures 4.3 and 4.4, it can be seen that the path length through the sheath will be

$$\Delta t_{\mathrm{Al}} = \sqrt{(x_{\mathrm{out}} - x_{\mathrm{in}})^2 + (y_{\mathrm{out}} - y_{\mathrm{in}})^2 + (z_{\mathrm{out}} - z_{\mathrm{in}})^2}, \tag{4.6}$$

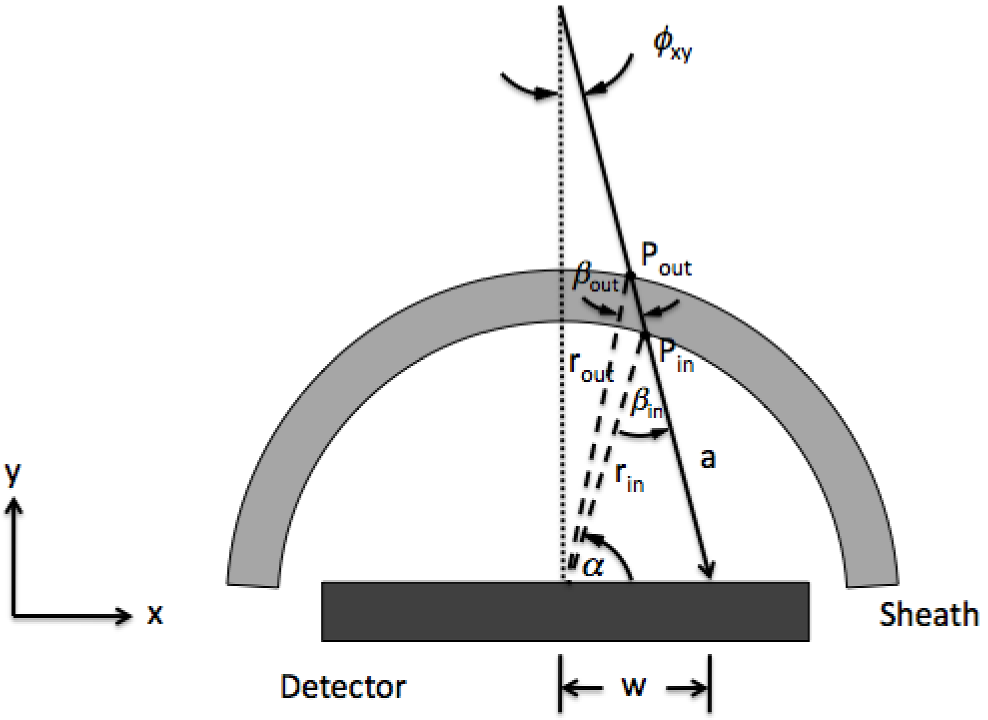

Figure 4.4: Mass thickness through sheath in x–y plane.

where the points P_{out} and P_{in}, with respective positions $(x_{\text{out}}, y_{\text{out}}, z_{\text{out}})$ and $(x_{\text{in}}, y_{\text{in}}, z_{\text{in}})$, are the intersection points of the x-ray with the outer and inner surface of the probe sheath, and are given by

$$\begin{aligned} x_{\text{in}} &= r_{\text{in}} \cos \alpha_{\text{in}}, \\ y_{\text{in}} &= r_{\text{in}} \sin \alpha_{\text{in}}, \\ z_{\text{in}} &= (R - y_{\text{in}}) \tan \theta, \end{aligned} \tag{4.7}$$

and

$$\begin{aligned} x_{\text{out}} &= r_{\text{out}} \cos \alpha_{\text{out}}, \\ y_{\text{out}} &= r_{\text{out}} \sin \alpha_{\text{out}}, \\ z_{\text{out}} &= (R - y_{\text{out}}) \tan \theta. \end{aligned} \tag{4.8}$$

Since the points P_{in} and P_{out} lie on the inner and outer radii of the probe sheath, the values for r_{in} and r_{out} are constant and equal to the inner and outer radii of the sheath, respectively. Therefore, there are three unknowns for each point P: two angles α and β, and one length a. The angle β in each of the triangles of Figure 4.4 can be determined by applying the Law of Sines to obtain

$$\begin{aligned} \beta_{\text{in}} &= \sin^{-1}\left(\frac{w}{r_{\text{in}}} \sin\left(\frac{\pi}{2} - \phi_{xy}\right)\right) = \sin^{-1}\left(\frac{w}{r_{\text{in}}} \cos \phi_{xy}\right), \\ \beta_{\text{out}} &= \sin^{-1}\left(\frac{w}{r_{\text{out}}} \sin\left(\frac{\pi}{2} - \phi_{xy}\right)\right) = \sin^{-1}\left(\frac{w}{r_{\text{out}}} \cos \phi_{xy}\right), \end{aligned} \tag{4.9}$$

and expressions for the remaining unknown angle α and length a can be found by applying the Law of Cosines [12]:

$$\begin{aligned} a_{\text{in}} &= \frac{w^2 - r_{\text{in}}^2}{w \cos(\frac{\pi}{2} - \phi_{xy}) - r_{\text{in}} \cos \beta_{\text{in}}} = r_{\text{in}} \frac{\left(\frac{w}{r_{in}}\right)^2 - 1}{\left(\frac{w}{r_{in}}\right) \sin \phi_{xy} - \cos \beta_{\text{in}}}, \\ a_{\text{out}} &= \frac{w^2 - r_{\text{out}}^2}{w \cos(\frac{\pi}{2} - \phi_{xy}) - r_{\text{out}} \cos \beta_{\text{out}}} = r_{\text{out}} \frac{\left(\frac{w}{r_{out}}\right)^2 - 1}{\left(\frac{w}{r_{out}}\right) \sin \phi_{xy} - \cos \beta_{\text{out}}}, \end{aligned} \tag{4.10}$$

and

$$\alpha_{\text{in}} = \cos^{-1}\left[\frac{1 + \left(\frac{w}{r_{in}}\right)^2 - \left(\frac{a}{r_{in}}\right)^2}{2\left(\frac{w}{r_{in}}\right)}\right], \tag{4.11}$$

$$\alpha_{\text{out}} = \cos^{-1}\left[\frac{1 + \left(\frac{w}{r_{out}}\right)^2 - \left(\frac{a}{r_{out}}\right)^2}{2\left(\frac{w}{r_{out}}\right)}\right].$$

Equations (4.7) through (4.11) can be used to evaluate Equations (4.5) and (4.6) for the path length Δt_{Al} and the resulting mass thickness $\bar{x}_{\text{Al}}$ of the probe sheath.

4.2 Integral XRAM Attenuation Model

Use of the exponential model for changes in intensity, given by Equation (2.1), accurately describes the nature of x-ray attenuation due to absorption by a material for a collimated, monoenergetic beam. The XRAM device, however, has a source with a broad spectrum of energy emitted at a wide angle, as described in Section 3.2.1. Using the source and detector characteristics provided by the manufacturers and the relative positions of each based on the geometry of the XRAM device, an expression for a physical model can be developed.

The basic geometry for the source and detector of the XRAM device is illustrated in Figure 4.5. To determine the intensity at the detector face, source characteristics are expressed in the cartesian coordinates (x, y, z); however, the layout of the source lends itself more naturally to a spherical coordinate system oriented relative to the axis of the x-ray tube, which is positioned at a fixed angle θ_0. Therefore, a relationship between the two coordinate systems is sought. Since the horizontal distance R between the centers of the source and detector is a constant, the source characteristics can be expressed as a function of x and z only in the form of $\theta(z)$ and $\phi(x)$, which can be determined from the geometry in Figure 4.5 and are given by

$$\theta(z) = \tan^{-1}\left(\frac{z}{R}\right), \tag{4.12}$$

and

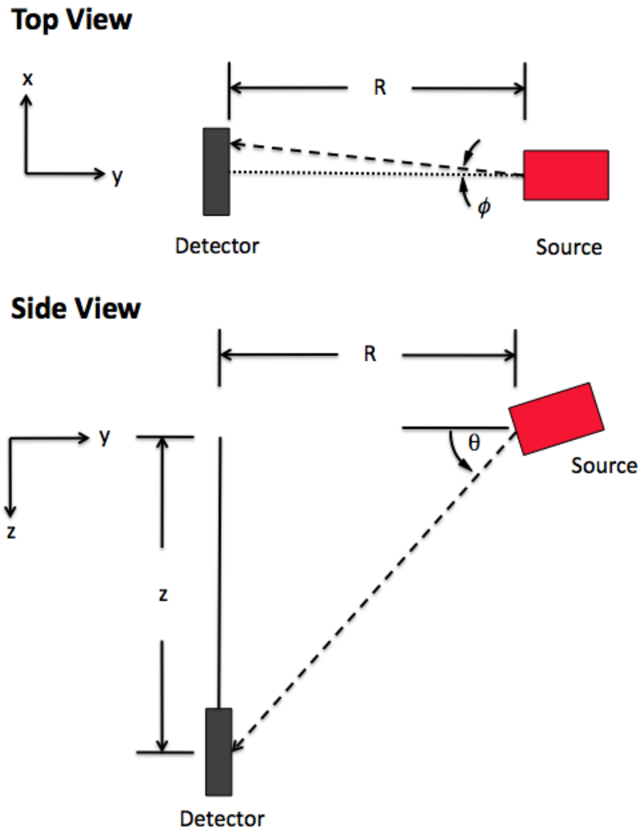

Figure 4.5: Basic source-detector geometry for the XRAM device.

$$\phi(x) = \tan^{-1}\left(\frac{x\cos\theta_0}{R}\right). \tag{4.13}$$

Even for a homogeneous sample, there will be additional materials present out of necessity to protect the x-ray source and detector from the environment that include a low density polyethylene (LDPE) window and aluminum alloy probe sheath. Therefore, the change in intensity due to absorption, denoted here by $\bar{\alpha}$, for x-rays passing through a series of materials can be written in the form

$$\begin{aligned}\bar{\alpha}(x,z,E) &= e^{-\frac{\mu_1}{\rho_1}(E)\bar{x}_1(x,z)}\; e^{-\frac{\mu_2}{\rho_2}(E)\bar{x}_2(x,z)}\;\ldots\; e^{-\frac{\mu_K}{\rho_K}(E)\bar{x}_K(x,z)}, \\ &= e^{-\sum\limits_{k=1}^{K}\frac{\mu_k}{\rho_k}(E)\,\bar{x}_k(x,z)},\end{aligned} \tag{4.14}$$

where K represents all the materials encountered between the source and detector.

Besides the change in intensity due to the absorption of x-rays, the x-ray intensity undergoes spherical spreading due to the wide angle of the source, which is proportional to $\frac{1}{r^2}$. In addition to the direct path, the contribution of x-rays scattered from the surrounding material can increase the intensity observed at the detector, and is accounted for with a buildup factor, $B(x,z,E)$.

The x-ray intensity observed at the detector is also affected by the spatial and spectral response of the source and detector. The source is assumed to have an energy independent beam pattern $D(\theta(z),\phi(x))$, and a spatially independent source spectrum $I_0(E)$. The detector has an energy dependent efficiency $\eta(E)$, which is assumed to not vary spatially across the face of the detector. The measured intensity for incident x-rays of energy E at a given point on the face of the detector, $\partial I(x,z,E)$, can be determined by the product of all these effects:

$$\partial I(x,z,E) = \frac{1}{r(x,z)^2} D(\theta(z),\phi(x))\, B(x,z,E)\, I_0(E)\, \eta(E)\, \bar{\alpha}(x,z,E). \tag{4.15}$$

The x-ray detector used on the XRAM device provides a single voltage output for a given measurement, effectively integrating the intensity over the energy range and area of the detector. For a detector with length l_0 and width w_0, the measured output at depth z can be determined by spatially and spectrally integrating Equation (4.15) to obtain

$$I(z) = \int\limits_{0}^{\infty} \int\limits_{-\frac{w_0}{2}}^{\frac{w_0}{2}} \int\limits_{z-\frac{l_0}{2}}^{z+\frac{l_0}{2}} \frac{1}{r(\xi,\zeta)^2} D(\theta(\zeta),\phi(\xi))\, B(\xi,\zeta,E)\, I_0(E)\, \eta(E)\, \bar{\alpha}(\xi,\zeta,E)\, d\zeta\, d\xi\, dE, \tag{4.16}$$

where ζ and ξ are variables of integration over the length and width of the detector, respectively. This represents the most general form of the measured change in intensity of the XRAM device, with no assumptions made about the source spectrum, sample composition, or relative size of the detector.

For the case of the XRAM device, the detector is rectangular with small dimensions l_0 and w_0 relative to R, the horizontal distance from the source. From Equation (4.13), it can be seen that for any value of $0 \leq x \leq \frac{w_0}{2}$, the ratio $\frac{x}{R} \ll 1$, so $\phi \ll 1$ for all x. With this approximation, the expression for the mass thickness through the aluminum probe sheath becomes independent of ϕ, which can be seen most simply by observing that the angle $\frac{\pi}{2} - \phi \approx \frac{\pi}{2}$ for $\phi \ll 1$. For a horizontally stratified sample, the mass thickness of each layer given by Equation (4.3) becomes independent of ϕ, since $\cos\phi \approx 1$ for $\phi \ll 1$. As a result, dependence on ϕ and x disappears from the integrand of Equation (4.16), so that the differential element $d\xi$ can be integrated to get w_0. The range of the vertical position z does not depend on l_0, so a small height approximation does not simplify the expression for $\theta(z)$ given in Equation (4.12). Therefore, rewriting r, D, B, $\bar{\alpha}$ and x_i as functions of the spatial variable z only, Equation (4.16) can be reduced to

$$I(z) = w_0 \int_0^{\infty} \int_{z-\frac{l_0}{2}}^{z+\frac{l_0}{2}} \frac{1}{r(\zeta)^2} D(\zeta)\, B(\zeta, E)\, I_0(E)\, \eta(E)\, e^{-\sum\limits_{k=1}^{K} \frac{\mu_k}{\rho_k}(E)\, \bar{x}_k(\zeta)}\, d\zeta\, dE. \tag{4.17}$$

For incident x-rays with energy in the Compton region, the mass attenuation coefficient is nearly independent of material composition. From Figure 2.6, it can also be seen that for the mass attenuation coefficient of the most relevant materials to the XRAM are much less sensitive to changes in energy in this range, such that over a sufficiently narrow energy band the coefficient can be assumed to be a constant value. Assuming the mass attenuation coefficient to be $\frac{\mu_0}{\rho_0}$, the spatial and energy dependence of Equation (4.17) can be integrated separately to yield

$$I(z) = w_0\, I_E \int_{z-\frac{l_0}{2}}^{z+\frac{l_0}{2}} \frac{1}{r(\zeta)^2}\, D(\zeta)\, B_z(\zeta)\, e^{-\frac{\mu_0}{\rho_0} \sum\limits_{k=1}^{K} \bar{x}_k(\zeta)}\, d\zeta, \tag{4.18}$$

where

$$I_E = \int_0^\infty B_E(E)\, I_0(E)\, \eta(E)\, dE, \tag{4.19}$$

and where it has been assumed that $B(z, E)$ is seperable and has the form

$$B(z, E) = B_z(z)\, B_E(E). \tag{4.20}$$

Although this simplifies the expression for the measured XRAM output, most of the source spectrum does not fall in this energy range, except after significant x-ray hardening from large sample thicknesses, or for use with a higher energy source.

4.3 Determining the Source Beam Pattern

To evaluate the integral in Equation (4.17), an accurate expression for the source beam pattern $D(z)$ is needed. Unfortunately, this information is not available through the manufacturer, since it is not relevant for its most common application in x-ray fluorescence, which utilizes spectral characteristics instead of changes in intensity. Direct experimental techniques using the existing XRAM test facilities were not possible due to the limited size of the shielded x-ray test area, preventing accurate wide-angle measurements from being obtained. However, since the beam pattern is the same for all of the data sets taken over a wide range of depths, details of $D(z)$ can be determined, though the task is made more difficult by the fact that $D(z)$ is in the integrand of Equation (4.17). With only a single, common beam pattern as a function of depth being sought and a large number of different data with significant overlaps in depth ranges, one method to determine $D(z)$ is by approximating it as a finite power series expansion of the form

$$D(z) \approx a_0 + a_1 z + a_2 z^2 + \cdots + a_{\mathrm{p}} z^p, \tag{4.21}$$

and then solving for the unknown coefficients by a least squares regression. By substitution of Equation (4.21) into Equation (4.17), a series form of the i^{th} data set $I^{(i)}(z)$ can be written as

$$I^{(i)}(z) \approx a_0 Q_0^{(i)}(z) + a_1 Q_1^{(i)}(z) + a_2 Q_2^{(i)}(z) + \cdots + a_{\mathrm{p}} Q_{\mathrm{p}}^{(i)}(z), \tag{4.22}$$

where

$$Q_j^{(i)}(z) = w_0 \int\limits_0^{\infty} \int\limits_{z-\frac{l_0}{2}}^{z+\frac{l_0}{2}} \frac{\zeta^j}{r(\zeta)^2}\, B(\zeta, E)\, I_0(E)\, \eta(E)\, e^{-\sum_{k=1}^{K} \frac{\mu}{\rho}{}_k^{(i)}(E)\, \bar{x}_k^{(i)}(\zeta)} d\zeta\, dE. \tag{4.23}$$

Following a standard method for a least squares regression for a general p^{th} order polynomial fit [13], the sum of the squares of the deviation σ between the i^{th} set of experimental data $I_{\text{exp}}^{(i)}(z)$ and the series expansion with the coefficients for all N_{data} sets of data is given by

$$\begin{aligned} \sigma &= \sum_{i=1}^{N_{\text{data}}} \left[I_{\text{exp}}^{(i)}(z) - I^{(i)}(z) \right]^2, \qquad (4.24) \\ &= \sum_{i=1}^{N_{\text{data}}} \left[I_{\text{exp}}^{(i)}(z) - (a_0 Q_0^{(i)}(z) + a_1 Q_1^{(i)}(z) + a_2 Q_2^{(i)}(z) + \cdots + a_{\text{p}} Q_{\text{p}}^{(i)}(z)) \right]^2. \end{aligned}$$

To find the coefficients that minimize the deviation between $I^{(i)}(z)$ and $I_{\text{exp}}^{(i)}(z)$, $d\sigma$ can be determined and set equal to zero, so that

$$d\sigma = \frac{\partial \sigma}{\partial a_0} da_0 + \frac{\partial \sigma}{\partial a_1} da_1 + \frac{\partial \sigma}{\partial a_2} da_2 + \cdots + \frac{\partial \sigma}{\partial a_{\text{p}}} da_{\text{p}} = 0. \tag{4.25}$$

But each term of Equation (4.25) is linearly independent, so each term can be set equal to zero, which yields

$$\begin{aligned}
\frac{\partial\sigma}{\partial a_0}&=\frac{\partial}{\partial a_0}\left[\sum_{i=1}^{N_\text{data}}\Big[I_\text{exp}^{(i)}(z)-\Big(a_0Q_0^{(i)}(z)+a_1Q_1^{(i)}(z)+a_2Q_2^{(i)}(z)+\cdots+a_\text{p}Q_\text{p}^{(i)}(z)\Big)\Big]^2\right]=0,\\
\frac{\partial\sigma}{\partial a_1}&=\frac{\partial}{\partial a_1}\left[\sum_{i=1}^{N_\text{data}}\Big[I_\text{exp}^{(i)}(z)-\Big(a_0Q_0^{(i)}(z)+a_1Q_1^{(i)}(z)+a_2Q_2^{(i)}(z)+\cdots+a_\text{p}Q_\text{p}^{(i)}(z)\Big)\Big]^2\right]=0,\\
\frac{\partial\sigma}{\partial a_2}&=\frac{\partial}{\partial a_2}\left[\sum_{i=1}^{N_\text{data}}\Big[I_\text{exp}^{(i)}(z)-\Big(a_0Q_0^{(i)}(z)+a_1Q_1^{(i)}(z)+a_2Q_2^{(i)}(z)+\cdots+a_\text{p}Q_\text{p}^{(i)}(z)\Big)\Big]^2\right]=0,\\
&\vdots\\
\frac{\partial\sigma}{\partial a_\text{p}}&=\frac{\partial}{\partial a_\text{p}}\left[\sum_{i=1}^{N_\text{data}}\Big[I_\text{exp}^{(i)}(z)-\Big(a_0Q_0^{(i)}(z)+a_1Q_1^{(i)}(z)+a_2Q_2^{(i)}(z)+\cdots+a_\text{p}Q_\text{p}^{(i)}(z)\Big)\Big]^2\right]=0.
\end{aligned}\tag{4.26}$$

Evaluating the derivatives of the system above for the j^th term gives

$$-2Q_j^{(i)}(z)\sum_{i=1}^{N_\text{data}}\Big[I_\text{exp}^{(i)}(z)-(a_0Q_0^{(i)}(z)+a_1Q_1^{(i)}(z)+a_2Q_2^{(i)}(z)+\cdots+a_\text{p}Q_\text{p}^{(i)}(z))\Big]=0,\tag{4.27}$$

where j is an integer $0\le j\le p$ (a total of $p+1$ terms). This equation can be rewritten in a form to solve for the unknown coefficients as

$$\begin{aligned}
&a_0\sum_{i=1}^{N_\text{data}}Q_0^{(i)}(z)Q_j^{(i)}(z)\;+\;a_1\sum_{i=1}^{N_\text{data}}Q_1^{(i)}(z)Q_j^{(i)}(z)\\
&+\;a_2\sum_{i=1}^{N_\text{data}}Q_2^{(i)}(z)Q_j^{(i)}(z)\;+\;\ldots\;+\;a_\text{p}\sum_{i=1}^{N_\text{data}}Q_p^{(i)}(z)Q_j^{(i)}(z)=\sum_{i=1}^{N_\text{data}}I_\text{exp}^{(i)}(z)Q_j^{(i)}(z).
\end{aligned}\tag{4.28}$$

This equation represents a linear system of equations with $p+1$ equations for $p+1$ unknowns. The analysis of the solution to this system is discussed in Section 6.2.2.

4.4 Determining the Density Gradient

To determine the density gradient of a given sample, the XRAM device collects a series of measurements $I(z_n)$ at N discrete depths $z_1, z_2, \ldots, z_N$. For a horizontally stratified sample, the total number of depths N also represents the maximum number of layers in the model and Equation (4.17) becomes

$$I(z_n) = w_0 \int_0^\infty \int_{z_n - \frac{l_0}{2}}^{z_n + \frac{l_0}{2}} \frac{1}{r(\zeta)^2} D(\zeta)\, B(\zeta, E)\, I_0(E)\, \eta(E)\, e^{-\sum\limits_{k=1}^{K} \frac{\mu_k}{\rho_k}(E)\, \bar{x}_k(\zeta)}\, d\zeta\, dE. \tag{4.29}$$

From Equation (4.29) it can be seen that the measured quantity at each z_n is on the left hand side of the equation and the unknown layer densities are inside the integrand on the right hand side, so the N system of equations will need to be inverted to determine the properties of each layer. To do this, numerical techniques must be used, in which case the continuous integrals of Equation (4.29) can be replaced by finite summations over energy and the depth,

$$\begin{aligned} I(z_n) = w_0 \sum_{i=1}^{M_i} \sum_{j=1}^{M_j} & \frac{1}{r(z_n + l_j)^2} D(z_n + l_j)\, B(z_n + l_j, E_i) \\ & \times I_0(E_i)\, \eta(E_i)\, e^{-\sum\limits_{k=1}^{K} \frac{\mu_k}{\rho_k}(E_i)\, \bar{x}_k(z_n + l_j)}\, \Delta l\, \Delta E, \end{aligned} \tag{4.30}$$

where

$$\begin{aligned} E_i &= E_0 + i\Delta E, & i &= 1, 2, \ldots, M_i, \\ z_n &= z_0 + nd, & n &= 1, 2, \ldots, N, \\ l_j &= j\Delta l - \frac{l_0}{2}, & j &= 1, 2, \ldots, M_j, \end{aligned} \tag{4.31}$$

with energy E_i, depth z_n, and vertical position on the detector face, l_j, having M_i, N and M_j discrete steps, respectively.

The density of each layer is contained in the mass thickness term of Equation (4.30), which appears in a summation within the argument of the exponential term.

As previously mentioned, the value K represents the total number of materials through which the x-ray passes between the source and detector. For a horizontally stratified sample, this will be the P_n layers up to and including the layer including the last point in the sample P_{out}, in addition to the probe sheath and the LDPE window. Therefore, this summation can be written as

$$\begin{aligned}\sum_{k=1}^{K} \frac{\mu_k}{\rho_k}(E_i)\,\bar{x}_k(z_n+l_j) = {} & \frac{\mu_{\text{LDPE}}}{\rho_{\text{LDPE}}}(E_i)\,\rho_{\text{LDPE}}\,\Delta t_{\text{LDPE}}(z_n+l_j) \\ & + \frac{\mu_{\text{Al}}}{\rho_{\text{Al}}}(E_i)\,\rho_{\text{Al}}\,\Delta t_{\text{Al}}(z_n+l_j) + \sum_{p=1}^{P_n} \frac{\mu_p}{\rho_p}(E_i)\,\rho_p\,\Delta t_p(z_n+l_j).\end{aligned} \tag{4.32}$$

The XRAM model can account for a single layer containing more than one material, such as a water-saturated sediment, if the inclusions are small enough relative to the thickness of the layer that it can be treated as an effective medium. For a two part composite layer, the effective density can be expressed as

$$\rho_{\text{eff}} = \upsilon\rho_1 + (1-\upsilon)\rho_2, \tag{4.33}$$

where ρ_1 and ρ_2 are the densities of the two materials, and υ is the volume fraction of *material 1*. In the case of liquid-saturated granular media, *material 1* denotes the fluid and υ is called the porosity.

For the case of a horizontally stratified layer, the physical properties are assumed to only be a function of depth. Thus, υ also represents the fraction of the total path length of the layer for an x-ray passing through *material 1*, and so the effective attenuation coefficient is simply

$$\mu_{\text{eff}}(E) = \upsilon\mu_1(E) + (1-\upsilon)\mu_2(E). \tag{4.34}$$

In the case of a water-saturated sediment, the two unknown properties of interest are the sediment density and the porosity, which can be expressed as unknown effective densities $\bar{\rho_1} = \upsilon\rho_1$ and $\bar{\rho_2} = (1-\upsilon)\rho_2$. In this form, the unknown densities can be used in Equation (4.32). With two unknowns per layer and N measurements, this limits the total number of layers to $\frac{1}{2}N$ with thickness $2d$.

Once the vector of unknown densities has been specified, a Newton-Raphson iteration method can be used to iterate for a solution of the system of equations given in Equation (4.30). The form of the Newton-Raphson method is

$$\mathbf{J}(\mathbf{x}^{(i)})\boldsymbol{\Delta}\mathbf{x} = -\mathbf{F}(\mathbf{x}^{(i)}), \tag{4.35}$$

where $\mathbf{x}^{(i)}$ is the i^{th} iteration of the vector of roots of the function $\mathbf{F}(\mathbf{x})$, $\boldsymbol{\Delta}\mathbf{x}$ is the correction to the guess $\mathbf{x}^{(i)}$, and $\mathbf{J}(\mathbf{x})$ is the Jacobian matrix. The recursion relation for multiple iterations is given by

$$\mathbf{x}^{(i+1)} = \mathbf{x}^{(i)} + \boldsymbol{\Delta}\mathbf{x}. \tag{4.36}$$

The Jacobian matrix depends on the partial derivates of $\mathbf{F}(\mathbf{x})$ according to

$$\mathbf{J}(\mathbf{x}) = \begin{bmatrix} \frac{\partial F_1}{\partial x_1} & \frac{\partial F_1}{\partial x_2} & \cdots & \frac{\partial F_1}{\partial x_N} \\ \frac{\partial F_2}{\partial x_1} & \frac{\partial F_2}{\partial x_2} & \cdots & \frac{\partial F_2}{\partial x_N} \\ \vdots & \vdots & \ddots & \vdots \\ \frac{\partial F_N}{\partial x_1} & \frac{\partial F_N}{\partial x_2} & \cdots & \frac{\partial F_N}{\partial x_N} \end{bmatrix}, \tag{4.37}$$

which can be approximated numerically by a 2-point centered finite difference derivative

$$\frac{\partial F_n}{\partial x_m} \approx \frac{F_n(x_m + \delta x_m) - F_n(x_m - \delta x_m)}{2\delta x_m}. \tag{4.38}$$

To use this method for the XRAM device, an appropriate function $\mathbf{F}(\boldsymbol{\rho})$ must be chosen so that the function has zeros for all N components with respect to the vector of unknown densities $\boldsymbol{\rho}$ when the N equations in Equation (4.30) are satisfied. To achieve this, $\mathbf{F}(\boldsymbol{\rho})$ can be defined as

$$F_n(\rho_m) = I_{\text{exp}}(z_n) - I(z_n, \rho_m), \tag{4.39}$$

which is simply the difference between the experimentally measured output $I_{\text{exp}}(z_n)$ and the modeled output given by Equation (4.30).

Applying Equations (4.35) through (4.38) to the XRAM by using $\mathbf{F}(\boldsymbol{\rho})$ yields a linear system that can be solved to determine the unknown layer densities, ρ_m:

$$\begin{bmatrix} \frac{\partial F_1}{\partial \rho_1} & \frac{\partial F_1}{\partial \rho_2} & \cdots & \frac{\partial F_1}{\partial \rho_N} \\ \frac{\partial F_2}{\partial \rho_1} & \frac{\partial F_2}{\partial \rho_2} & \cdots & \frac{\partial F_2}{\partial \rho_N} \\ \vdots & \vdots & \ddots & \vdots \\ \frac{\partial F_N}{\partial \rho_1} & \frac{\partial F_N}{\partial \rho_2} & \cdots & \frac{\partial F_N}{\partial \rho_N} \end{bmatrix} \begin{bmatrix} \Delta\rho_1 \\ \Delta\rho_2 \\ \vdots \\ \Delta\rho_N \end{bmatrix} = - \begin{bmatrix} F_1(\rho_m) \\ F_2(\rho_m) \\ \vdots \\ F_N(\rho_m) \end{bmatrix}, \tag{4.40}$$

where the recursion relation is

$$\rho_m^{(i+1)} = \rho_m^{(i)} + \Delta\rho_m, \tag{4.41}$$

and the partial derivatives in Equation (4.40) can be determined by

$$\frac{\partial F_n}{\partial \rho_m} \approx \frac{F_n(\rho_m + \delta\rho_m) - F_n(\rho_m - \delta\rho_m)}{2\delta\rho_m}. \tag{4.42}$$

The solution for the unknown densities can be obtained by solving Equation (4.40) for the vector of density changes $\boldsymbol{\Delta\rho}$ for each iteration until the difference between the modeled output and measured output is sufficiently small. The linear system of Equation (4.40) can be expressed in the form $\mathbf{Ax} = \mathbf{y}$ with a solution for $\mathbf{x}$ obtained by multiplying $\mathbf{y}$ by the inverse of $\mathbf{A}$. This solution can be more generally defined for an m x n matrix by the Moore-Penrose pseudoinverse matrix, given by [14]

$$\mathbf{x} = \left(\mathbf{A}^T\mathbf{A}\right)^{-1}\mathbf{A}^T\mathbf{y}. \tag{4.43}$$

In the cases where the matrix $\mathbf{A}$ is singular, nearly singular or ill-conditioned, the inverse or pseudoinverse does not exist or is otherwise meaningless. For such ill-posed problems, Equation (4.43) is not applicable. Unfortunately, this is the case for the linear system given in Equation (4.40) for typical samples and depths to be investigated by the XRAM device, suggesting that standard linear system techniques will not yield a meaningful solution. This occurs because the sensitivity of the intensity relative to changes in the sample properties of a given layer, appearing in the Jacobian matrix in Equation (4.40), decreases significantly as the x-ray passes through additional layers. As a result, the sensitivities are small and relatively constant at even moderate depths, creating a rank deficient matrix.

Treatment of an ill-posed system such as the one encountered in the XRAM model can be treated by regularization, a process by which the inverse of a matrix $\mathbf{A}^{-1}$ is replaced by a family of approximate inverses $\mathbf{C}_h$ with $h > 0$. Here, h is known as the regularization parameter, and is defined such that $\mathbf{C}_h$ approaches A^{-1} as h approaches zero [15]. One form of an approximate inverse $\mathbf{C}_h$ can be achieved by addition of a small multiple of the identity matrix $\mathbf{I}$ to the pseudoinverse, such that

$$\mathbf{C}_h = \left(\mathbf{A}^T\mathbf{A} + h^2\mathbf{I}\right)^{-1}\mathbf{A}^T. \tag{4.44}$$

Using this expression in place of the pseudoinverse yields [16]

$$\mathbf{x} = \left(\mathbf{A}^T\mathbf{A} + h^2\mathbf{I}\right)^{-1}\mathbf{A}^T\mathbf{y}, \tag{4.45}$$

which is known as *Tikhonov matrix regularization.*

The rank deficiency of the linear system encountered in Equation (4.40) at moderate depths suggests that additional information is needed to find a unique solution. By the process of regularization, this additional information is gained by prescribing the smoothness of the solution, which is contained in the parameter h (a larger value of h implies a smoother solution). The use of regularization is not limited only to rank deficient system, but can be applied generally to ill-posed systems, since numerically ill-conditioned systems are treated the same way as singular systems [15].

4.5 Uncertainty Analysis

To determine how well the modeled results and experimental data compare, the difference between the true value and the modeled value can be characterized by the measured error. However, this true value is not accurately known, so the actual error can be estimated by the *uncertainty*, which if estimated correctly, can provide the range within which the true value can be found.

Before determining the uncertainty, it is important to consider the underlying errors that lead to the differences between the observed and true values. There are two main types of errors: precision error and bias error, which are illustrated in Figure 4.6. The scatter in the data is quantified by the precision error, which includes the effects of errors relating to repeatability, resolution, and variations in

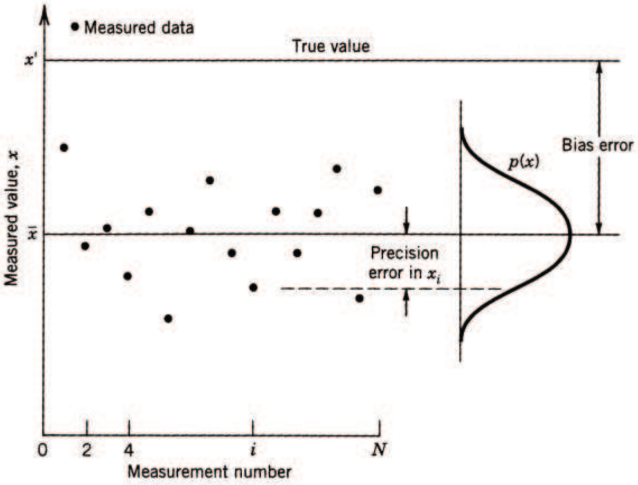

Figure 4.6: Precision error and bias error in measured data [13].

operating and environmental conditions. Since the variations in the data resulting from precision error are not constant, this error can best be quantified by statistical means. On the other hand, bias error remains constant during a series of measurements, and thus cannot be quantified by statistical techniques. Although some times difficult to detect, the best way to quantify and ultimately reduce the bias error is by calibration.

For quantifying the precision error, statistics for finite sample sizes can be considered. For N measurements, the sample mean and sample variance are given by

$$\bar{x} = \frac{1}{N}\sum_{i=1}^{N} x_i, \tag{4.46}$$

and

$$S_x^2 = \frac{1}{N-1}\sum_{i=1}^{N}\left(x_i - \bar{x}\right)^2, \tag{4.47}$$

respectively, where x_i are the i^{th} measured values and S_x is the sample standard deviation. When these N measurements are repeated multiple times, a normal distribution of mean values would be expected. By the central limit theorem, the resulting variation can be described by the standard deviation of the mean [17],

$$S_{\bar{x}} = \frac{S_x}{\sqrt{N}}. \tag{4.48}$$

The precision interval within a $P\%$ probability for a measurement x can then be given by $\bar{x} \pm t_{\nu,P} S_{\bar{x}}$, where $t_{\nu,P}$ is a weighting for finite sample sizes with ν degrees of freedom for a $P\%$ interval, given by the *Student-t distribution* [18]. The degrees of freedom, ν, is determined by the total number of independent measurements available for estimating a value. For large ν, $t_{\nu,P}$ reduces to the value τ obtained using infinite statistical methods, which can be evaluated using

$$P = \frac{1}{\sqrt{2\pi}} \int_{-\tau}^{\tau} e^{-\frac{\beta^2}{2}} d\beta, \tag{4.49}$$

where P is the probability that $-\tau \leq \beta \leq \tau$, with

$$\beta = \frac{x - \bar{x}}{\sigma}, \tag{4.50}$$

and

$$\sigma^2 = \lim_{N \to \infty} \frac{1}{N} \sum_{i=1}^{N} (x_i - \bar{x})^2 . \tag{4.51}$$

To estimate the total uncertainty u_x in a measurement or model simulation of the quantity x, the contributions of individual error elements ϵ_k can be combined using a root-sum-square (RSS) method:

$$u_x = \sqrt{\epsilon_1^2 + \epsilon_2^2 + \cdots + \epsilon_k^2}. \tag{4.52}$$

To determine the uncertainty in a dependent variable y due to the uncertainty in an independent variable x at the point (x_0, y_0), let

$$y_0 \pm u_y = f\left(x_0 \pm u_x\right), \tag{4.53}$$

where the resulting uncertainty in y can be written as

$$u_y = \left(\frac{dy}{dx}\right)_{x=x_0} u_x, \tag{4.54}$$

where the derivative in parenthesis is the *sensitivity* of y with respect to x at $x = x_0$. To represent uncertainty due to bias error, u_x can be expressed simply as a constant bounded range. For precision error, u_x can be determined statistically at $P\%$ probability by

$$u_x = t_{\nu,P} S_{\bar{x}}. \tag{4.55}$$

In the more general case where $\mathbf{x}$ and $\mathbf{y}$ are vectors (where both are discrete functions of another variable such as depth), the uncertainty in $\mathbf{y}$ due to an uncertainty in $\mathbf{x}$ is given by

$$\mathbf{u_y} = \mathbf{J}(\mathbf{x})\mathbf{u_x}, \tag{4.56}$$

where $\mathbf{J}(\mathbf{x})$ is the Jacobian matrix, given by Equation (4.37). Equations (4.55) and (4.56) will be used in Section 6.2.3 to evaluate the uncertainty in XRAM device measurements.

Chapter 5

Experimental Procedures and Apparatus

Two basic types of experiments were conducted to calibrate the XRAM device and measure density gradients in known test samples to evaluate its accuracy. The first type of experiment involves spectral analysis of the source intensity and sample attenuation. This was performed to verify the exponential model of x-ray hardening that occurs through a sample with known physical properties described by Equation (2.1), and to determine the source spectrum, which is necessary to model the change in intensity measured at the XRAM detector according to Equation (4.17). The second type of experiment uses the XRAM detector and provides only information on the averaged intensity over the energy spectrum and area of the detector face. This data is used to determine the beam pattern of the source, and to evaluate the performance of the XRAM as a measurement device, including its sensitivity and precision.

5.1 Spectrum Analysis

5.1.1 Experiment Setup

To investigate the spectral behavior of the Eclipse II source, an external x-ray detection system was used, the layout of which is illustrated in Figure 5.1. In this experiment, an XR-100CR silicon diode x-ray detector was placed in the irradiated

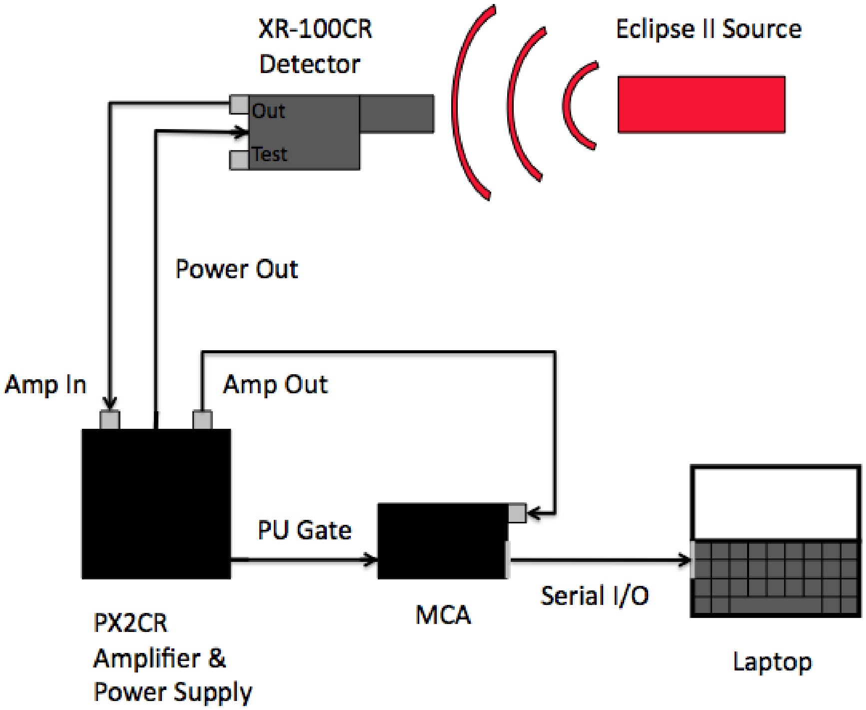

Figure 5.1: Experimental layout for source spectrum measurement.

region of the Eclipse II source. The detector is connected to a PX2CR amplifier unit, which provides power and receives data from the XR-100CR. The PX2CR amplifies the output and sends it to a portable multichannel analyzer (MCA). The MCA takes the amplified raw signal from the PX2CR, as well as input from a pile-up (PU) gate. The processed signal out of the MCA is sent by a serial I/O to a laptop computer, where the data can be analyzed using software provided by the MCA manufacturer called PMCA.

The PMCA software provides the data in the form of a histogram, displaying the total number of electron-hole pairs counted by the detector that occur in each energy bin. The size of the bins are determined by the dynamic range and number of bits sampled. The energy range is adjusted by changing the amplitude of the signal from the MCA, so adjusting the gain level can be used to obtain a wide dynamic range. However, this also means that the energy range has been scaled, and needs to be calibrated to an absolute reference. Although the output could be

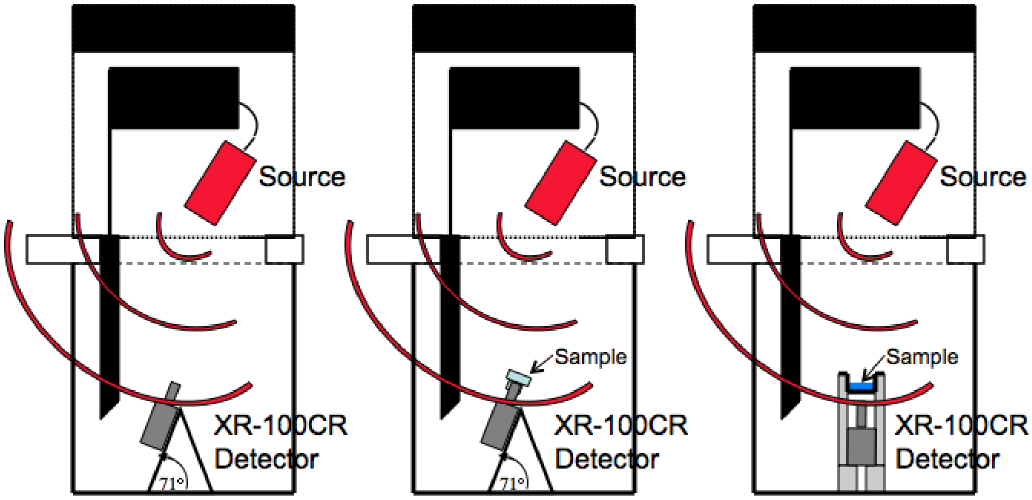

Figure 5.2: Experimental setup for XRAM source spectrum measurement (left), and spectral changes due to aluminum (center) and liquid samples (right).

calculated based on the gain applied to the detector output (both in the PX2CR and in the PMCA software), a more accurate way is to calibrate the energy axis by using the spectral characteristics produced by the source target, which in the case of the Eclipse II are the K_α and K_β characteristics emitted by silver at 22.1 keV and 25.0 keV, respectively. In this manner, the PMCA software allows for the x-ray energy at the spectrum to be characterized at the detector.

To test the Eclipse II source while mounted in the XRAM device, the XR-100CR must be configured in a way to obtain accurate measurements. To do this, the XR-100CR was placed at an angle of 71° relative to the horizontal using a triangular mount facing the Eclipse II source, inside of a plastic circular housing, as shown in the left panel of Figure 5.2. Although the Eclipse II source was aligned at an angle of 62.5° relative to the horizontal, 71° was the closest angle possible without being obstructed by the probe sheath. To determine the source spectrum emitted from the XRAM device, the test is conducted with no sample between the source and detector, except for the ambient air.

In addition to a nominal spectral measurement, the attenuated spectra for different samples can be measured using a similar configuration. By measuring the

Figure 5.3: (a.) XR-100CR detector with PX2CR amplifier and power supply, and (b.) x-ray detector components (courtesy of Amptek, Inc.).

thickness of the sample in addition to the resulting spectrum, the exponential model given by Equation (2.1) can be used to model the changes between the nominal and attenuated spectra. Spectra for three samples were investigated: 6061 aluminum alloy, distilled water and methanol. The setup for testing the aluminum alloy, shown in the center panel of Figure 5.2, is the same as for the nominal spectral measurement except that the sample (indicated by light blue in the figure) is attached to the end of the XR-100CR. To attach the sample in a repeatable manner without damaging the detector, a 2.51 cm long cylindrical aluminum standoff was fit over the end of the detector and connected to the sample.

To ensure accurate meaurements of liquid samples, the modified configuration illustrated in the right panel of Figure 5.2 was used. In this setup, the XR-100CR was aligned vertically inside of a tube (represented by the light gray structure around the XR-100CR in the figure), which was attached to a styrofoam container held above the detector to contain the liquid sample. In this manner, different thicknesses of liquid samples could be investigated, and the thickness could be determined simply by measuring the height of the liquid.

5.1.2 X-ray Spectrum Detector

The Si-PIN XR-100CR x-ray detector used for spectral analysis mentioned above, and illustrated in Figure 5.3, operates by counting electron-hole pairs created when x-rays pass through a silicon target, which occur at a rate of one per 3.62 eV of incident energy on average. To provide sufficient sensitivity, a high bias voltage of

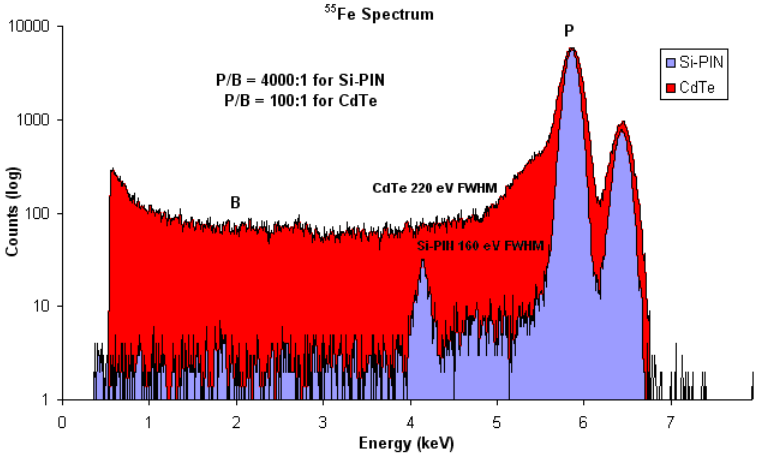

Figure 5.4: Comparison of Fe Spectrum using Si-PIN (blue) and CdTe (red) detectors (courtesy of Amptek, Inc.).

100 V to 200 V must be applied across the silicon. In order to maintain this voltage with minimal losses, the system is actively cooled and keep near -55^{o}C. If heating above -20^{o}C occurs, the detector performance decreases and becomes temperature dependent [19].

For the applicable energy ranges, the silicon diode detector has a higher energy resolution than a CdTe detector, which is also available in the XR-100CR device. To illustrate the difference in performance, Figure 5.4 shows the spectrum for iron up to 7 keV, taken with a Si-PIN and CdTe detector by the manufacturer. In the figure, values for the P/B (peak-to-background) ratio are given, which in decibels is equivalent to the signal-to-noise (SNR) of the detector. Based on the P/B ratios given by the manufacturer over this energy range, the SNR of the Si-PIN detector is 72 dB, compared to 40 dB for the CdTe detector.

In both cases displayed in Figure 5.4, the SNR has been improved using a rise-time descrimination (RTD) circuit. This circuit located in the PX2CR removes noise and artificial peaks due to partial charge collection resulting from partially undepleted portions of silicon in the detector. Although the SNR of the Si-PIN is 32 dB higher at low energies, the efficiency of the detector in stopping x-rays (and thereby creating electron-hole pairs that can be measured by the XR-100CR) has a strong energy dependence, as shown in Figure 5.5. Although nearly 100% at 10 keV,

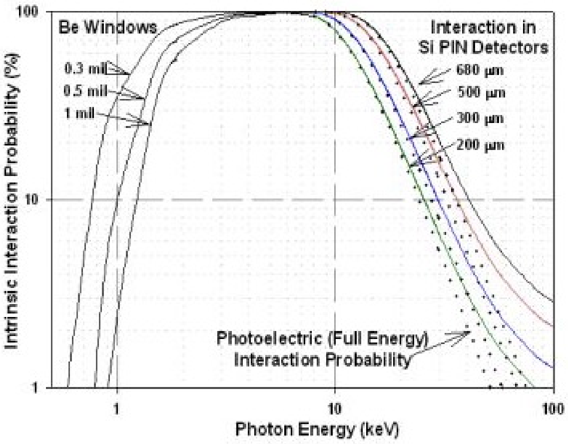

Figure 5.5: Probability of photon interaction in Si-PIN detector (courtesy of Amptek, Inc.).

the Si-PIN detector efficiency decreases logarithmically beyond this energy band. In addition, the detector efficiency operates by detecting photoelectric interactions only, which occur in a lower percentage of the x-ray interactions as absorption from Compton scattering becomes significant. At energies below 2 keV, absorption of x-rays by the beryllium window dominates, preventing most of the incident energy from interacting with the silicon.

In addition to the limited energy bandwidth of the XR-100CR, both the detector (XR-100CR) and its amplifier (PX2CR) are limited by the rate of incident photons (intensity of incident x-rays) that the system can accurately count. The PX2CR is limited by its ability to resolve individual pulses from incident photon interactions in the XR-100CR. This effect can be seen in Figure 5.6, which shows the difference between the input count rate (ICR) and the resulting output count rate (OCR). From the figure, it can be seen that as ICR increases, the resulting OCR is no longer linearly related, and actually reaches a maximum point beyond which increasing the ICR does not increase the OCR. Additionally, when high rates of incident photons interact with the XR-100CR, too many electron hole-pairs occur in the silicon before the charge collection can be reset, resulting in artifacts at energies above that of the incident x-rays. This effect, known as charge pileup, can

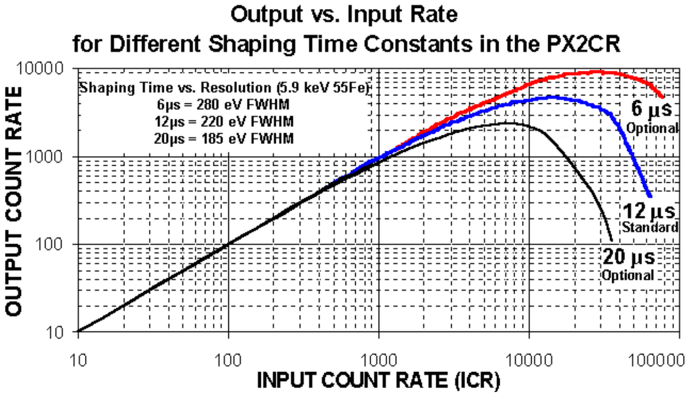

Figure 5.6: PX2CR Output Count Rate v. Input Count Rate (courtesy of Amptek, Inc.).

be reduced by using the PU gate on the PX2CR.

As previously mentioned, the output produced by the PMCA software is a histogram showing the number of counts occurring in each energy bin. To obtain the best statistical distribution for a given data set, the highest number of counts is needed. This can be obtained by operating near the maximum OCR, which for the standard 12 μs shaping is 4000–5000 counts per second (cps) according to Figure 5.6. To produce this optimal range of OCR, an ICR of 10000–20000 cps is needed. The ICR can be adjusted by varying the current to the Eclipse II source and the distance between the source and detector.

5.2 Attenuation Measurements

5.2.1 Experiment Setup

The experimental setup for attenuation measurements, shown in Figure 5.7, represents the primary configuration of the XRAM device to investigate samples with unknown density gradients. Direct measurements of the attenuated spatially and spectrally averaged x-ray intensity are made as a function of depth for a given sample, and from these measurements the density at each depth can be determined. These measurements utilize the onboard CdTe x-ray detector instead of the XR-100CR spectrum analyzer. The CdTe detector is moved down the length of the

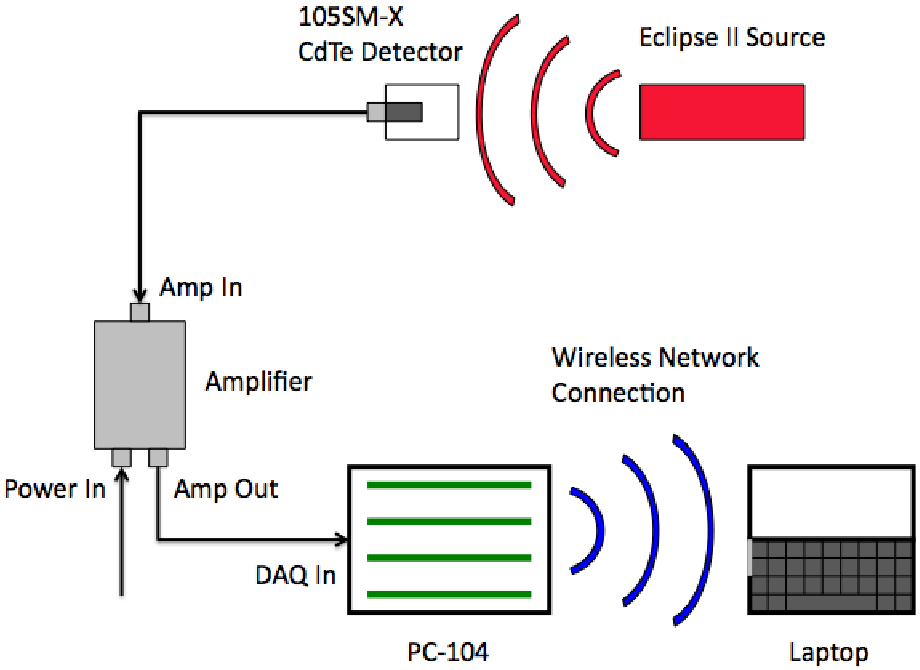

Figure 5.7: Experimental layout for attenuation measurements.

probe by a stepper motor, transmitting the measured voltage through a high gain amplifier located at the base of the probe. The data is stored on an embedded PC/104 computer, which runs a LabVIEW virtual instrument algorithm that controls the signal gain, number of steps, number of averages taken at each step, and time delay between measurements, in addition to creating the output file with the averaged voltage measurements. When the testing is complete, the raw data is then transferred using a wireless network connection to a laptop for analysis. This process is illustrated in Figure 5.7.

Three different sample types were investigated using this setup to determine the density measurement capabilities of the XRAM, as illustrated in Figure 5.8. The first sample type (left panel of Figure 5.8) consists of a single liquid, either water or methanol. For a single homogenous liquid, there should be no gradient and a single known density should be measured. By looking at two liquids with different densities, the effects of sample density and depth on the accuracy can be evaluated.

The second sample type (middle panel of Figure 5.8) is a liquid layer above a

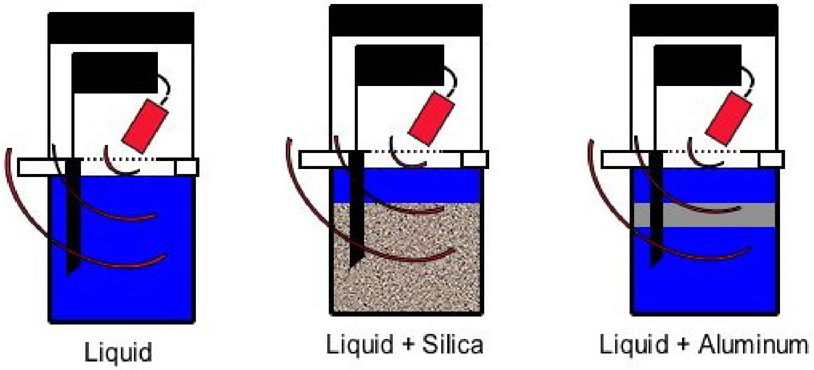

Figure 5.8: XRAM attenuation experimental configurations for the three different types of samples investigated: liquid only (left), liquid-saturated glass beads (center), and liquid with aluminum alloy layer (right).

monodisperse liquid-saturated glass bead sediment. This case is similar to the type of sample that would be encountered on the ocean floor, and should demonstrate a similar range and accuracy as would be observed at sea. Although the chemical composition of the water-saturated glass bead sediment gives an accurate representation of ocean sediments, the purpose of the XRAM device is to investigate density gradients, which are not present due the homogeneous structure of the glass bead sample. A third sample type shown in the right panel of Figure 5.8 consisting of a homogenous liquid layer with a single solid layer of 6061 aluminum alloy evaluates the ability of the XRAM device to distinguish between the properties of two distinctly different layers, which is an important task in determining the density gradient of the seafloor.

5.2.2 Experiment Apparatus

Although all the measurement apparatus used to take data are part of the XRAM device and detailed in Chapter 3, the samples being investigated required several components not previously described. To contain the samples, a 9.46 L plastic container 23.2 cm deep was used. These dimensions allow the XRAM device to rest on top of the container while the probe sheath is fully submerged and

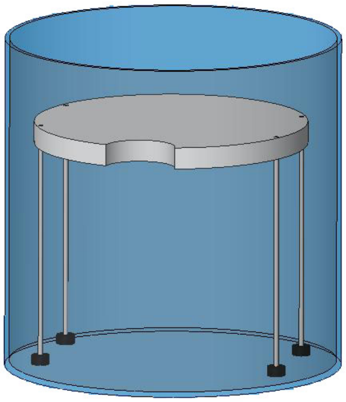

Figure 5.9: 6061 aluminum alloy layer and supporting structure for the attenuation measurement experiment setup.

perpendicular to any density gradients present in the sample.

In all cases, the container was filled with a liquid, but also included solid samples for the cases shown in the center and right panels of Figure 5.8. For the case of the aluminum alloy layer, a structure was needed to keep it horizontal and suspended at a given depth. The structure consists of a 1.34 cm thick layer of 6061 aluminum alloy supported by 4 stainless steel legs, as illustrated in Figure 5.9. Each leg consists of an assembly of male-female round threaded standoffs attached to a rubber foot, which allows for the height to be adjusted while keeping the aluminum alloy layer level. The aluminum alloy layer is circular to match the shape of the container, with a semicircular notch to fit around the XRAM probe sheath. The composition of 6061 aluminum alloy, given in the left panel of Table 5.1, consists of between 95.85% and 98.61% elemental aluminum by weight, as well as trace amounts of magnesium, silicon, copper, chromium and several other metals. Although mostly aluminum by weight, the alloying components of 6061 aluminum alloy have noticeably different x-ray attenuation properties, which will be discussed in more detail in Section 6.1.2.

For the water-saturated sediment samples, soda-lime glass beads with a mean density of 2.5 g/cc and a mean diameter of 2.2 mm (± 0.2 mm maximum deviation) were used. The composition of the soda-lime glass provided by the manufacturer is

Component	**% min**	**% max**
Aluminum, Al	95.85%	98.61%
Magnesium, Mg	0.80%	1.20%
Silicon, Si	0.40%	0.80%
Iron, Fe	—	0.70%
Copper, Cu	0.15%	0.40%
Chromium, Cr	0.04%	0.35%
Zinc, Zn	—	0.25%
Manganese, Mn	—	0.15%
Titanium, Ti	—	0.15%
Other	—	0.15%

Component	**% min**	**% max**
SiO_2	60%	70%
Na_2O	12%	18%
CaO	15%	20%
MgO	1%	4%
Al_2O_3	1%	5%
Other	—	2%

Table 5.1: Chemical composition (by weight) of the 6061 aluminum alloy (left) and the soda-lime glass beads (right) used in the attenuation measurement experiment [20].

given in the right panel of Table 5.1, and gets its name from the three main components: silica (glass), sodium oxide (soda) and calcium oxide (lime). To prepare the sample, the beads were mixed with water in the container and filled to the necessary height. Unlike the aluminum alloy layer, no supporting structure is necessary for the water-saturated glass bead sample.

Chapter 6

Data Analysis

6.1 Spectrum Analysis

6.1.1 Source Spectrum

As discussed in Section 5.1.1, the source spectrum of the Eclipse II source used in the XRAM is needed to accurately determine the amount of energy attenuated by the sample being investigated. The experimental measurements of the source spectrum, however, are affected by the spectrum analyzer sensitivity to different energy bands and the incident intensity. Figure 6.1 shows the measured source spectrum using the XR-100CR on the left. To obtain the actual spectrum emitted by the source, the inverse of the XR-100CR efficiency (shown in Figure 5.5) is used to correct the amplitude variation caused by the XR-100CR. This correction is shown in the right panel of Figure 6.1.

As described in the previous chapter, the amplitude of the spectrum is recorded as a histogram, counting the number of interactions that occur in each energy bin. The magnitude of this is a function of the intensity (count rate) of the source and how long the data are recorded for. Since the important aspect of the spectrum analysis is the energy dependent changes in amplitude, the normalized amplitudes are given in Figure 6.1. The small variations in amplitude in the left panel of the figure show the statistical distribution of the uncertainty in the raw data. However, these variations are only observed for energies above 30 keV, which is the maximum amount of energy possible from a source with an applied potential of 30 kV. These interactions are not from the source itself, but artifacts from charge

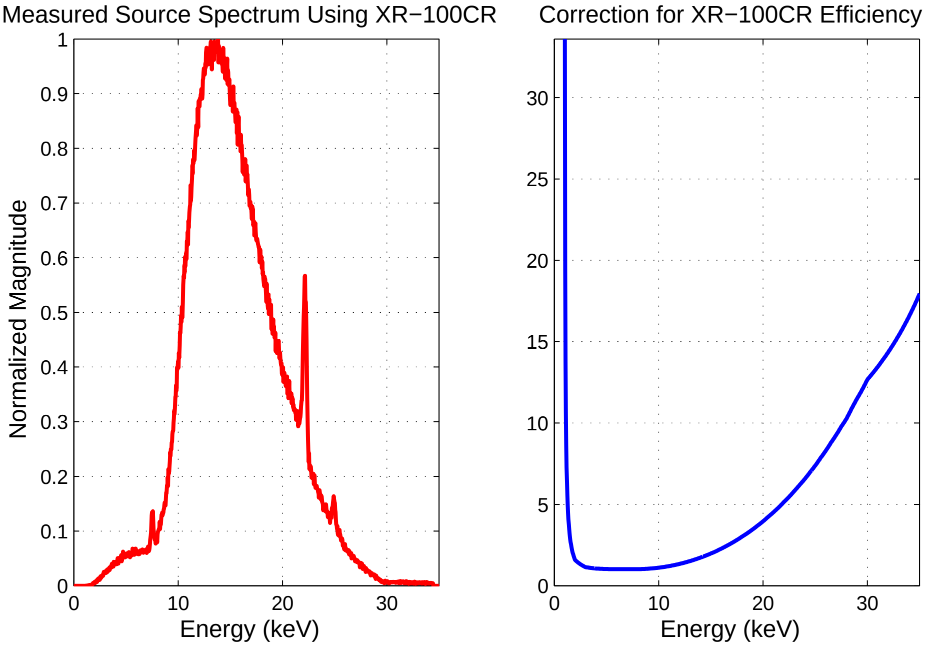

Figure 6.1: XRAM source spectrum as measured by XR-100CR with LDPE window present at 71° (left), and correction for XR-100CR efficiency (right).

pileup in the XR-100CR. Although the PX2CR includes techniques to reduce the effects of pileup, there are still small amounts (approximately 1% or less of the peak value) that appear in the data, although the exact amount depends on the intensity of the incident x-rays.

Although these high energy artifacts are a relatively small part of the spectral measurement and only slightly larger than the amplitude variations seen at other energies due to statistical uncertainty, this effect is amplified by the large correction needed for the XR-100CR due to the poor performance near 30 keV. It can be seen from the right panel of Figure 6.1 that this error between 30 and 35 keV is increased by a factor of 13 to 18 times relative to the data at 10 keV and below. The effect of this can be seen by comparing the plots in red showing the raw spectrum (left) and corrected spectrum (right) in Figure 6.2. This will become more significant as more of the sample of is analyzed, since the spectrum will harden as the x-rays travel through more material. As a result, the lower energies will be attenuated much

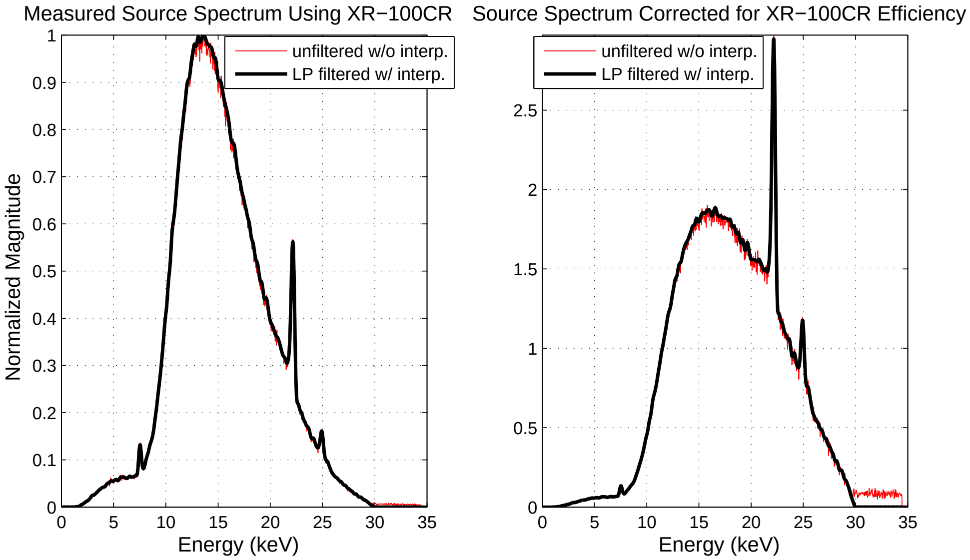

Figure 6.2: Effects of high energy artifacts on XRAM source spectrum as measured by XR-100CR (left), and with correction for XR-100CR efficiency (right).

more rapidly and the error due to the higher energy pileup artifacts will make up a much larger proportion of the spectral power.

To minimize this error, data was collected at the lowest x-ray intensity possible, and taken over a time period of several minutes to maintain an acceptable statistical variation in the amplitude measurements. Since it is physically impossible for the source to produce x-rays above 30 keV, the spectrum above this value was assumed to be zero. It was assumed that the slope in the vicinity of 30 keV should be constant, since the effects of hardening over a very narrow energy band will be nearly uniform. Therefore, a linear extrapolation of the spectrum above the 25 keV characteristic and below the artifact noise floor was performed, and used to extend over the range where the artifact noise floor occurred. In addition, a lowpass (LP) filter was applied to the modified spectrum to remove the high frequency oscillations (due to random statistical fluctuations distributed about the mean) before accounting for the XR-100CR efficiency. This adjusted spectrum is shown in black in Figure 6.2.

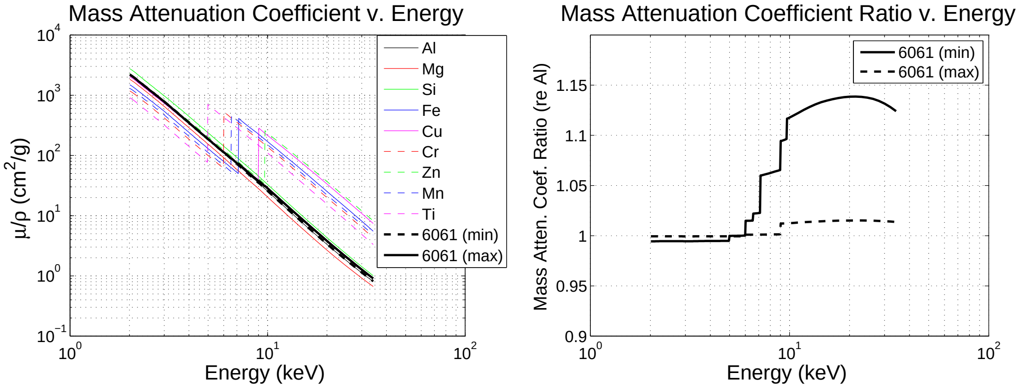

Figure 6.3: Mass attenuation coefficients for 6061 aluminum alloy and alloying elements (left), and relative increase due to alloying elements for minimum and maximum concentrations (right).

6.1.2 Forward Spectral Modeling

With the spectral characteristics of the source known, it is possible to track the spectral changes that occur through a material of known composition and thickness. This is important because components used to protect the x-ray source and detector from damage, including the aluminum alloy probe sheath and LDPE window, attenuate the x-rays in addition to the sample of interest and must be accounted for. To model the results of these tests (illustrated in the center and right panels of Figure 5.2), the initial source spectrum I_0 is simply hardened according to the exponential attenuation model given by Equation (2.1) for the measured sample thickness and compared to the experimentally observed spectrum. The mass attenuation coefficient for each sample tested (water, methanol and 6061 aluminum alloy) were obtained from the National Institute of Standards and Technology (NIST) Physical Reference Data, which contains a compiled list of x-ray mass attenuation coefficients for the first 92 elements of the periodic table [10].

Although mass attenuation coefficients of pure elements are given by NIST, values for mixtures such as 6061 aluminum alloy are not. However, the mass attenuation coefficient for a mixture can be determined by a summation of the product of the mass fraction and mass attenuation coefficient for each component, as given by Equation (2.2). For 6061 aluminum alloy, the bulk density is 2.70 g/cc and the

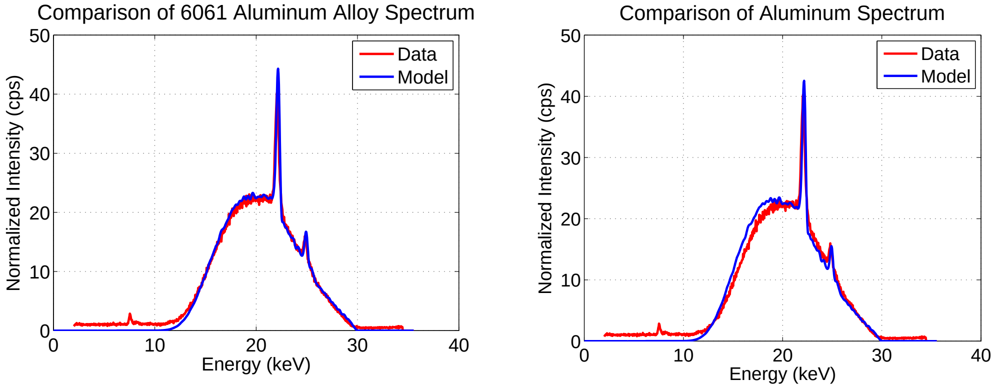

Figure 6.4: Normalized spectral amplitude for 6061 aluminum alloy sample, modeled using mass attenuation coefficients for maximum concentration of alloying elements (left) and minimum concentrations (right).

composition by weight is given in the left panel of Table 5.1.

The mass attenuation coefficient for 6061 aluminum alloy with maximum and minimum concentrations of alloying elements, and each of the individual components, are illustrated in the left panel of Figure 6.3. Although the composition by weight of the alloying elements is very small, most of the components have mass attenuation coefficients that are an order of magnitude larger than that of pure aluminum over the energy range of interest. As a result, these alloying elements contribute a significant amount to the absorption of x-rays even in small concentrations. In the right panel of Figure 6.3, the ratio of the mass attenuation coefficient for the maximum and minimum concentrations for 6061 aluminum alloy are given relative to the values for pure aluminum. It can be seen that the maximum concentration varies by up to 14%, while the minimum concentration, which does not contain most of the highly absorptive alloying elements, varies at most by only 1.5%.

The effects of the difference can be seen in the spectral modeling of 6061 aluminum samples, as demonstrated in Figure 6.4. To model the experimental data of the 0.130 cm thick 6061 aluminum alloy sample, the source spectrum was attenuated by the mass attenuation coefficients for the maximum concentration of 6061 aluminum alloy in the left panel of the figure, and by pure aluminum in the right panel. It can be seen that the mass attenuation coefficient for the 6061 aluminum alloy with maximum concentration of alloy elements very accurately represents the

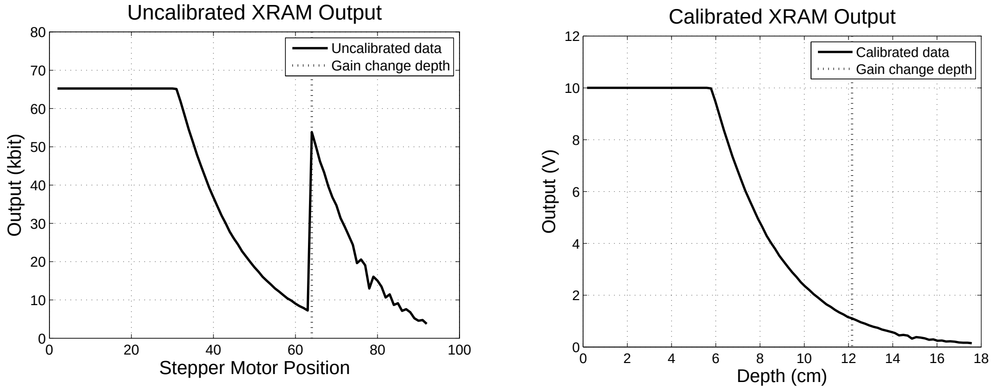

Figure 6.5: Uncalibrated (left) and calibrated (right) XRAM output.

spectral characteristics of the measured data, whereas the pure aluminum model appears noticeable softer (more lower energy content) than the measured results.

6.2 Attenuation Measurements

As described in Section 5.2, the primary configuration of the XRAM device is for measurements of the total energy attenuated by the sample taken at a series of depths, from which the density gradient can ultimately be determined. To obtain these results, several steps must be taken to convert the raw output recorded by the XRAM device into useful density gradient information. The first step is applying calibration curves to convert the raw data recorded in bits as a function of stepper motor position into output voltage versus probe depth. After calibration, the raw data can then be processed, which is accomplished by applying a lowpass filter and removing any saturated portions of the data. Finally, the processed data can be compared to the XRAM model for determining the source beam pattern or inverted to find the density gradient.

6.2.1 Processing XRAM Output

There are two main steps involved with processing the output from the XRAM device to obtain an accurate representation of the attenuation of a given sample as a function of depth. First, a calibration of the raw data as illustrated by

Variable	**Description**	**Value**
N	Total number of depth increments	92
Δd	Incremental depth change	0.195 cm
d_{tot}	Total change in depth	17.78 cm
d_0	Initial depth	2.40 cm

Table 6.1: Tabulated values for depth calibration.

the representative set shown in Figure 6.5 is needed. These data show the internally referenced values within the XRAM device hardware in the left panel of the figure (bits and stepper motor position), and the external values they represent in the right panel of the figure (measured output voltage and probe depth). Second, the data are processed so that only the attenuated measurement is represented, and effects due to noise and voltage saturation are removed.

The desired abscissa is probe depth, which must be determined from the raw measurement given simply by the stepper motor position. Each stepper motor position is equally spaced, and begins each data set at the same predefined position, with all depth measurements taken from the center of detector. Thus, the depth at the n^{th} step, d_n, can be determined by a linear calibration of the form

$$d_n = (n - 1)\Delta d + d_0, \tag{6.1}$$

where d_0 is the initial depth of the first stepper motor position, and Δd is the depth change between stepper motor positions. The specific values of Δd and d_0 are determined by the number of steps taken over the total depth range and the arbitrary selection of the zero depth reference point, respectively. The zero depth reference point used for all measurements is relative to the bottom of the XRAM, which is chosen so that in an ocean environment, the sample being investigated would begin at a depth of 0 cm. The values used for the depth calibration are summarized in Table 6.1.

For the ordinate, it is desired to determine the output voltage from the raw measurement given simply by the number of bits stored from the data acquisition system. For comparison of the data with the XRAM model, the full-scale voltage

Variable	**Description**	**Value**
V_{FSR}	Full-scale voltage range	10 V
m	Number of bits (A/D conversion)	16
G	Gain factor	1 to 8
x_0	Vertical bias (in bits)	324 bits ($G = 1$)
		33 bits ($G = 8$)

Table 6.2: Tabulated values for voltage calibration.

range starts at zero, so that zero output voltage corresponds to the case when no source is present. This can be accounted for by removing any bias present before the source is turned on for each of the gain settings. The general linear voltage calibration is given by

$$y = Q(x - x_0), \tag{6.2}$$

where

$$Q = \frac{1}{2^m}\frac{V_{\mathrm{FSR}}}{G}, \tag{6.3}$$

V_{FSR} is the full-scale voltage range, G is the gain, x is the number of bits as determined by the m-bit A/D conversion, and x_0 is the bias (in bits) observed in the raw data when the source is off. To determine this bias, XRAM data was recorded at each probe depth with the source turned off for different gain settings. These values, as well as all the other relevant parameters, are summarized in Table 6.2.

The purpose of the different gain settings is to increase the resolution of the raw data, which is accomplished by decreasing Q in Equation (6.3). Physically, Q represents the smallest voltage increment that can occur, due to the change of a single bit in the raw data. The tradeoff for higher resolution is a decreased dynamic range, since there are still 2^m points in the data. However, the higher resolution is useful for data taken at larger probe depths, since the overall dynamic range is small due to the high attenuation at these depths.

To effectively process the calibrated data and remove any extraneous parts of the measurements that are not related to the x-ray attenuation of the physical system or response of the XRAM device, the general nature of the data must be

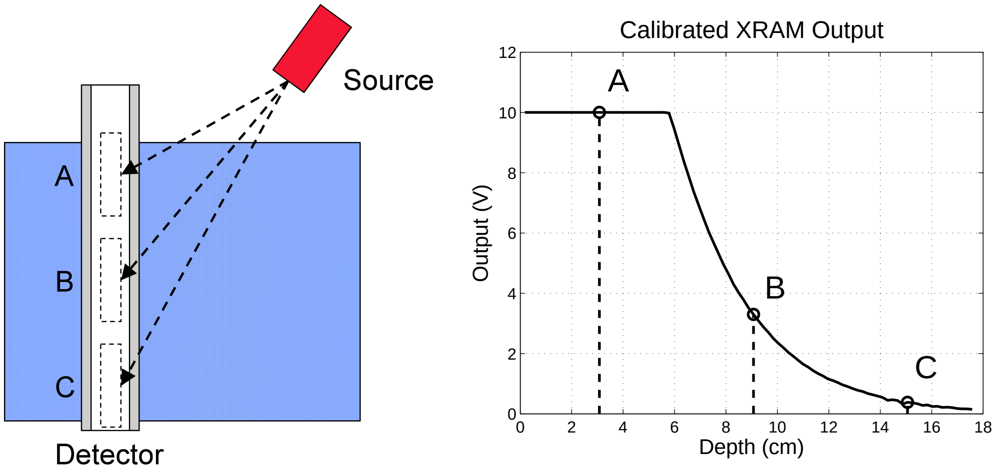

Figure 6.6: Illustration of the relationship between detector position (left) and calibrated XRAM output voltage (right).

understood. The relationship between the detector positions and the measured data at that depth are illustrated in Figure 6.6. From this illustration, it can be seen that the measured attenuated signal decreases rapidly with depth, due to the combination of increasing sample thickness and geometric spreading of the source energy. This rapid change in amplitude with depth makes it difficult to obtain data across the entire depth range, especially depths at or around the point A. At point A, the voltages are beyond saturation. At depths around that of point B, which lies within the dynamic range, the data has a high signal-to-noise ratio yielding the most repeatable results. However, once the detector has reached depths near that of point C, the large decrease in amplitude leads to a decreased signal-to-noise ratio. In addition, at such large depths the detector (which is mounted on a thin plastic arm), tends to oscillate more significantly when the depth is changed by the stepper motor, leading to inaccuracies.

To correct for these effects in the region around point C shown in Figure 6.6, the calibrated XRAM data is lowpass filtered to remove any artifacts in the data due to noise or vibration. However, simply applying a low-pass filter to the calibrated data is not helpful for two main reasons. First, the data is generally monotonically decreasing, so that the voltage at the initial depth position is much higher than than that at the final depth position. Since the data is a discrete set of points

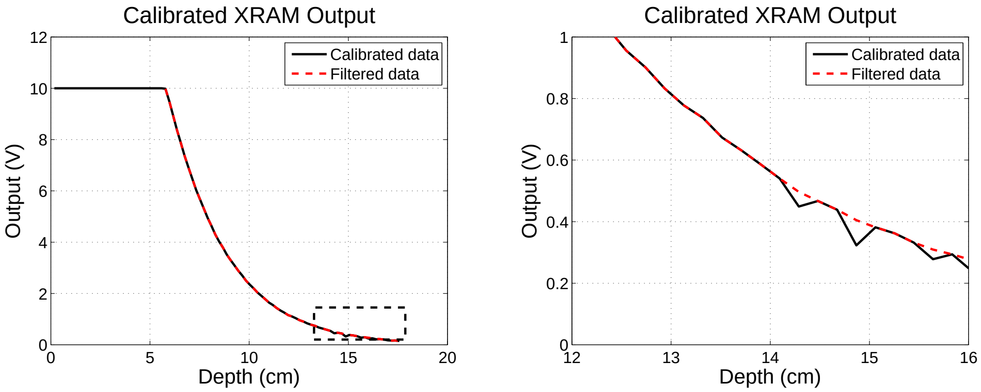

Figure 6.7: Calibrated XRAM output voltage comparison between filtered and unfiltered data (left) and a zoomed in view (right).

with a finite spatial range, any type of discrete Fourier transformation technique used in applying a lowpass filter will treat the data as one period, repeating the pattern for higher depths, resulting in a discontinuity between the voltages at the initial and final depths. Applying a lowpass filter to such a discontinuous jump will distort the data significantly, since the resulting data includes the lower spatial frequencies from both the calibrated data plus that of a step function, due to the discontinuity between the initial and final depths. Second, the observed fluctuations in the measured data, like the ones highlighted in the right panel of Figure 6.7, are sharp drops in the voltage which are not centered about the mean value.

Due to these problems, a modified method of applying a lowpass filter was used for the calibrated XRAM data. This process involves three main steps: identifying and correcting any discontinuities in the data, creating a modified set of data for filtering purposes, and then applying the filter to the modified data, from which the unmodified filtered data can be extracted.

To identify if there are any discontinuities in the data, the first derivative of the data is calculated by finite difference methods, and checked for any large changes corresponding to the large slope changes when there is a spike present in the data). To remove these discontinuities from the data, the first derivative of the nearest acceptable data point is taken and used to interpolate the data where the spikes occurred. In the case of relatively homogeneous materials, linear interpolation works very well, but in the case of more inhomogeneity more elaborate schemes must

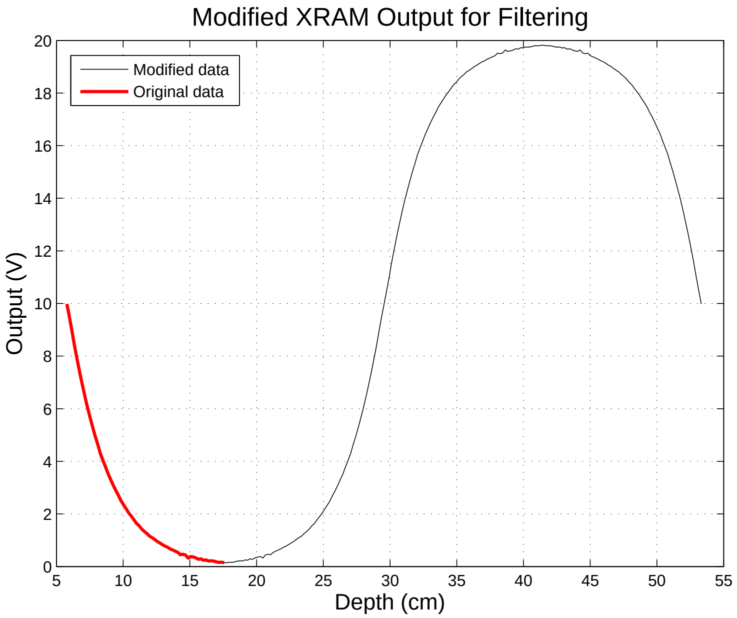

Figure 6.8: Calibrated XRAM output voltage (solid red line), and in modified form for filtering (solid black line).

be used, such as higher order interpolation or filtering the first derivative results to obtain the slope at each corresponding depth.

Once any discontinuities occurring in the data have been removed, a modified form of the data is sought for the purposes of minimizing any artificial effects from using discrete (spatial) frequency analysis techniques. In this case, the original data is padded with flipped and rotated sets of the original data, so that the slope and value match at the initial and final depths of the modified data set, as shown in Figure 6.8. A lowpass filter can then be applied to this modified data set, and then the portion consisting of the original data can then be extracted. The results of this filtering method are illustrated in Figure 6.7.

6.2.2 Comparison of XRAM Model

To compare the measured data, a relative model was used rather than an absolute model. This was accomplished by normalizing the modeled data amplitude

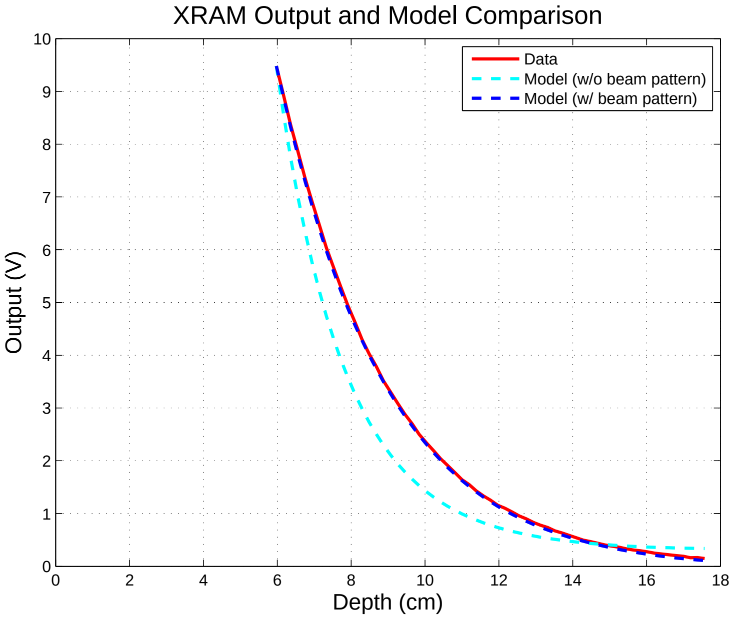

Figure 6.9: Comparison of XRAM output (solid red line) and modeled data with (dark blue dashed line) and without (light blue dashed line) beam pattern.

at a particular depth, as illustrated in Figure 6.9. Although more elaborate methods could be applied to theoretically model the incident x-ray intensity and therefore a corresponding model amplitude, the uncertainty in the buildup factors used in the model make this difficult to do in an accurate and repeatable manner. As will be discussed later in this section, this is especially true at higher depths, where the sensitivity of the measurement to the density gradient becomes very low, meaning that even a small variation the in data would appear as a large (erroneous) change in density when inverted. Thus, a single point normalization provides the most accurate way to match the amplitude of the specific data set.

From Figure 6.9, it can be seen that although the data aligns in the vicinity of the depth were the amplitude was normalized, the modeled behavior does a poor job of tracking the changes with depth. This problem is characteristic of all the data sets, and was assumed to be due to the beam pattern of the source. If this assumption is correct, then the beam pattern would create variations in amplitude with respect to the depth the data was taken at, and would be common to all data

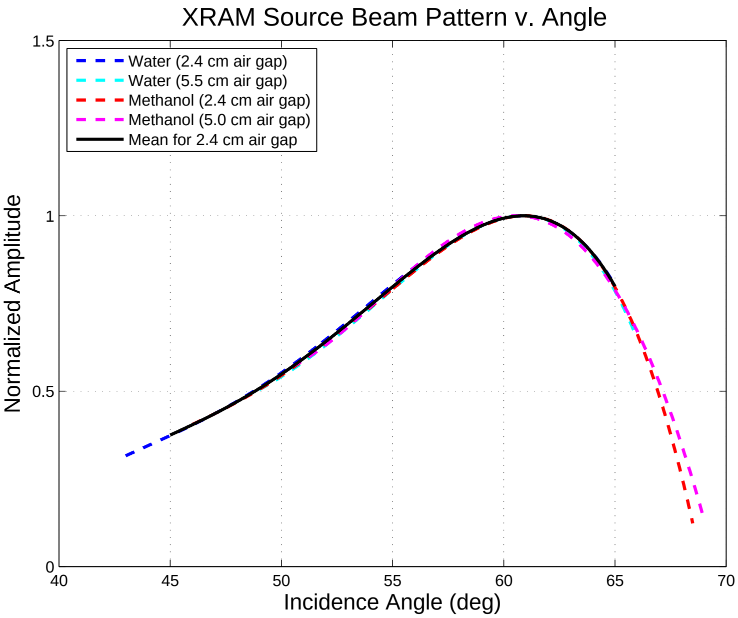

Figure 6.10: Normalized source beam pattern as a function of incidence angle obtained from typical water samples of different air gap sizes, typical methanol samples of different air gap sizes, and the mean value.

sets, regardless of the samples tested.

The beam pattern for a given set of data can be calculated from Equation (4.28), the results of which are illustrated in Figure 6.10 for water and methanol samples with different size air gaps. It can be observed that all the data sets appear to yield the same beam pattern as would be expected, though the total depth ranges are different depending on how much the signal amplitude varies within the dynamic range of the XRAM device due to the effects of attenuation and geometric spreading for a given sample. Thus, a sample like methanol with lower attenuation and a larger air gap would provide the best results at higher depths, but would saturate at lower depths. Conversely, a higher attenuation sample like water with a smaller air gap provides the best results at lower depths, but is completely attenuated (relative to the sensitivity of the XRAM device) at higher depths. Thus, using the range of samples and air gaps illustrated in the figure provides a wide range of depths that could be used for a variety of different samples.

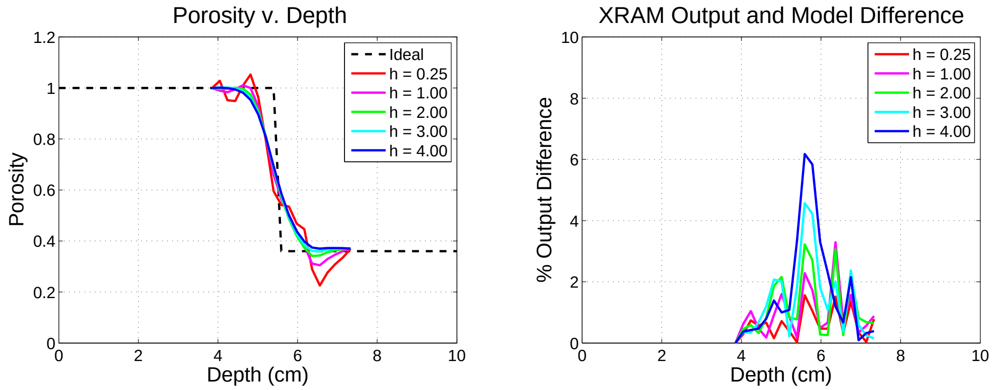

Figure 6.11: Results of inversion for sample layer porosity using Tikhonov regularization for an idealized step change in porosity for different values of the regularization parameter h (left), and the corresponding difference between the measured and modeled output (right).

The water and methanol samples used to determine the XRAM beam pattern consist of a single homogeneous material of known density and composition, so that the only unknown in the model is the angular dependent amplitude common to all data sets. In this situation all the sample physical parameters needed as input into the XRAM model are known, allowing the data to be fully modeled. However, in most cases of interest, the gradient of either the density or porosity is unknown. In this situation, an initial estimate of the unknown quantity at each depth can be iterated until the model matches the measured data. This means that a single unknown physical property is actually a vector of unknown values, since the density at each modeled layer needs to be determined, resulting in a linear system of equations of the form $\mathbf{Ax} = \mathbf{b}$ as described in Section 4.4.

To solve this system, a technique known as Tikhonov regularization can be used, which is described by Equation (4.45), where h is the regularization parameter that prescribes the smoothness of the solution. Although using the form of Equation (4.45) allows a meaningful solution to be obtained to the linear system, the challenge then becomes choosing a value for h that applies the right amount of smoothness. Theoretical means exist for determining the optimal regularization parameter by minimizing the error, although these are complicated by trying to quantify the error, and can be affected by noise perturbations of the right-hand side. As a result,

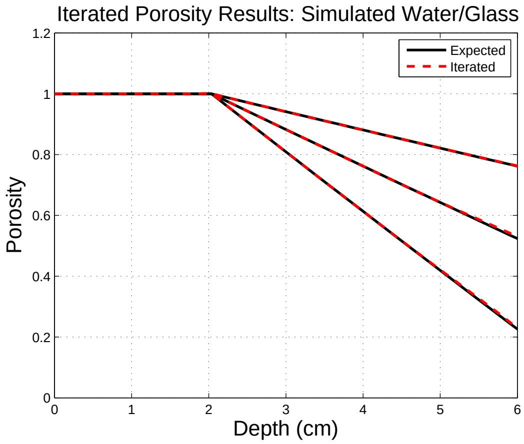

Figure 6.12: Results of inversion for sample layer porosity using Tikhonov regularization for three simulated linear gradients of different slopes, with the simulated input gradient shown in solid black and the final iteration of the porosity inversion shown in dashed red.

specialized cases are often developed for specific families of singular systems and heuristic approaches are often used [15].

Since the general form of the linear system used for the XRAM model has the same source of the singular or nearly-singular behavior in the system arising from the decreasing sensitivity at higher depths for all samples, simple trial-and-error provided the best means for a near-optimal regularization parameter than could be used for a wide range of data. Through this process, which is illustrated in Figure 6.11 for an idealized density gradient, a value of $h = 2.00$ was determined. In the figure, it can be seen that for values of h larger than 2.00, the results are smoothed too much so that abrupt changes in density or porosity would not be accurately detected. However, for values of h smaller than 2.00, the system becomes more singular in its behavior, producing large artificial oscillations in the inverted data.

To verify the inversion process, simulated data was created using the XRAM model given by Equation (4.17) with an arbitrary density gradient, which was then inverted using Tikhonov regularization techniques to obtain a "measured" density gradient. Figure 6.12 shows the results of three different linear gradients of a simulated water/glass mixture. For this representative case, the density of the water and

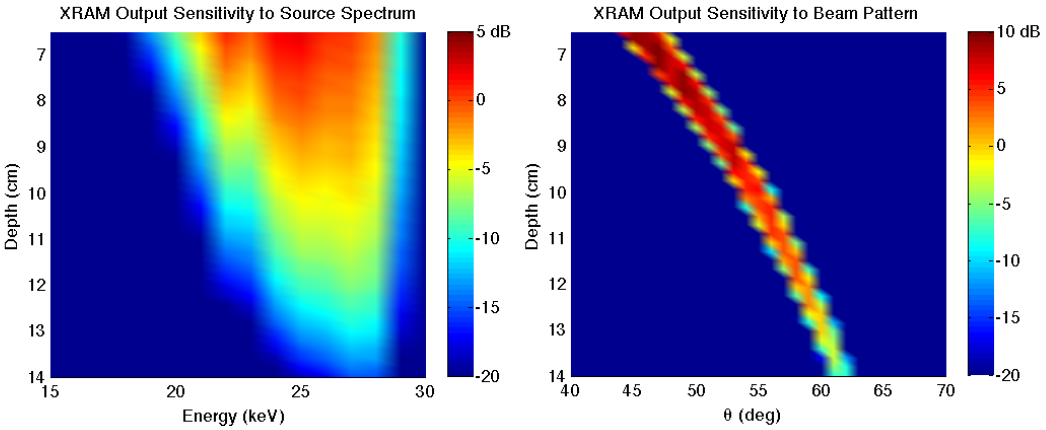

Figure 6.13: Typical XRAM output voltage sensitivity to source spectrum amplitude (left) and source beam pattern amplitude (right), given in dB re 1 V.

the glass beads was assumed to be fixed with the depth-dependent porosity being unknown, which is the same case as the water-saturated glass beads measured using the XRAM device. In the figure, there is excellent agreement between the simulated data and measured output porosity for each of the three gradients illustrated.

6.2.3 Measurement Sensitivity and Uncertainty

The sensitivity of the output to different input variables can be very useful in understanding the behavior of the measurement system. In the case of the XRAM device, both the input and output variables of interest are depth dependent, so from Equation (4.56) the sensitivity is given by the Jacobian matrix. To determine the response of the output parameter to a given input parameter, the XRAM model developed in Section 4.2 was used. To calculate each of the partial derivatives in the Jacobian matrix, the numerical finite difference expression given by Equation (4.38) can be utilized.

Several important sensitivities are shown in Figures 6.13 and 6.14, which are simply graphical representations of the Jacobian matrix expression given in Equation (4.37). In the figures, the input parameter is shown on the abscissa, and the colors show the corresponding sensitivity, which varies with the depth given along the ordinate.

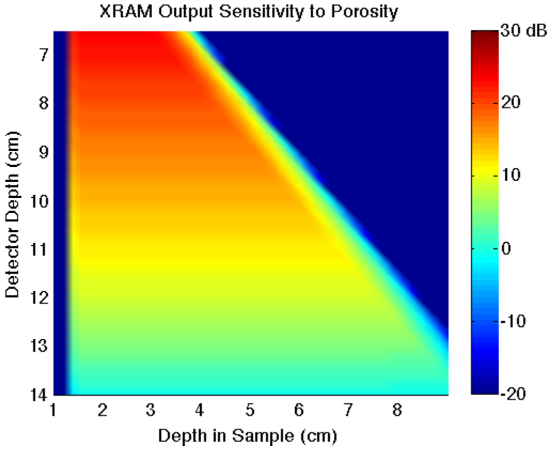

Figure 6.14: Typical XRAM output voltage sensitivity to sample layer porosity, given in dB re 1 V.

The most important input parameters relating to the XRAM output voltage and inverted porosity are the sensitivity of the XRAM output voltage with respect to the source spectrum, beam pattern, and sample layer density. A typical example of the sensitivity of XRAM output voltage to the source spectrum is shown in the left panel of Figure 6.13. At the lowest detector depth position shown (which corresponds to the beginning of the non-saturated measured data), the XRAM output is only sensitive to x-ray energies above 20 keV, as a result of x-ray hardening. At this depth, the energies at which the output is most sensitive to changes in amplitude occur near 22 and 25 keV, where the emission lines for the silver target in the Eclipse II source occur. As the detector depth increases, the source spectrum continues to harden, shifting the peak sensitivity to higher energies, while the overall magnitude of the sensitivity decreases significantly.

An example of the sensitivity of XRAM output to the experimentally determined source beam pattern is shown in the right panel of Figure 6.13. Variation in the beam pattern, which was assumed to only be a function of angle, affects the XRAM output voltage over a narrow band of specific combinations of depth and angle, due to the geometric relationship between these two parameters, given by Equation (4.12). As with the source spectrum, the magnitude of the sensitivity decreases with increasing detector depth.

Figure 6.14 illustrates a typical example of the sensitivity of the XRAM output voltage to the porosity of each sample layer. Note that for a layer with two components, such as a water-saturated glass bead mixture, the sensitivity with respect to the total layer density is simply scaled by $\frac{\partial \beta}{\partial \rho_{\mathrm{tot}}} = \frac{-1}{\rho_{\mathrm{g}} - \rho_{\mathrm{w}}}$. From this plot, it can be seen that the sensitivity remains constant at a given detector depth for all the sample layer depths, up to a sample depth beyond which the sensitivity is zero (limited to -20 dB re 1 V in the figure for representation in dB). This sample depth corresponds to the last layer in which x-rays reaching the detector will pass and is illustrated in Figure 4.1 as layer p.

In the same manner as the other XRAM output voltage sensitivities, it can be observed that the sensitivity decreases as the detector depth increases. Based on the noise levels observed during experimentation, the threshold needed for regularization techniques to be successful is about 10 dB re 1 V, or 3.16 V. Since the sensitivity is the change in output voltage due to a change in porosity (which is dimensionless), this means that a 1.0% change in porosity corresponds to a 31.6 mV change in the observed output voltage at this threshold.

From Figure 6.14 it can be seen that this decrease affects each sample layer in a nearly uniform manner. Thus, the relative sensitivity of the output voltage from a particular layer is dominated by the presence of all the other layers the x-rays pass through between the source and detector. When trying to invert these measurements for the sample layer properties, the large uniform decrease in sensitivity observed in Figure 6.14 is the primary limitation on the depth into a sample that can be investigated.

Chapter 7

Results

The measured Eclipse II source spectrum is shown in black in Figure 7.1 after performing the analysis described in Section 6.1.1 to account for the effects of the x-ray spectrum analyzer. Although measurements from the manufacturer are not available under the same operating procedures as described in Section 5.1.1, the source spectrum shown in the figure can be verified by comparing the predicted at-

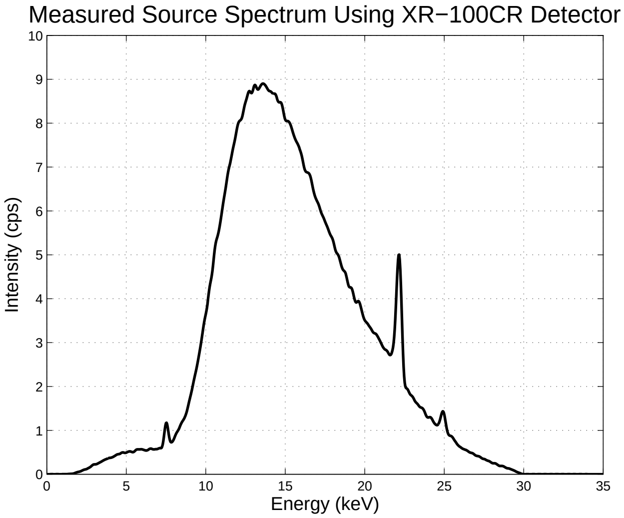

Figure 7.1: Measured Eclipse II source spectrum obtained using the XR-100CR detector.

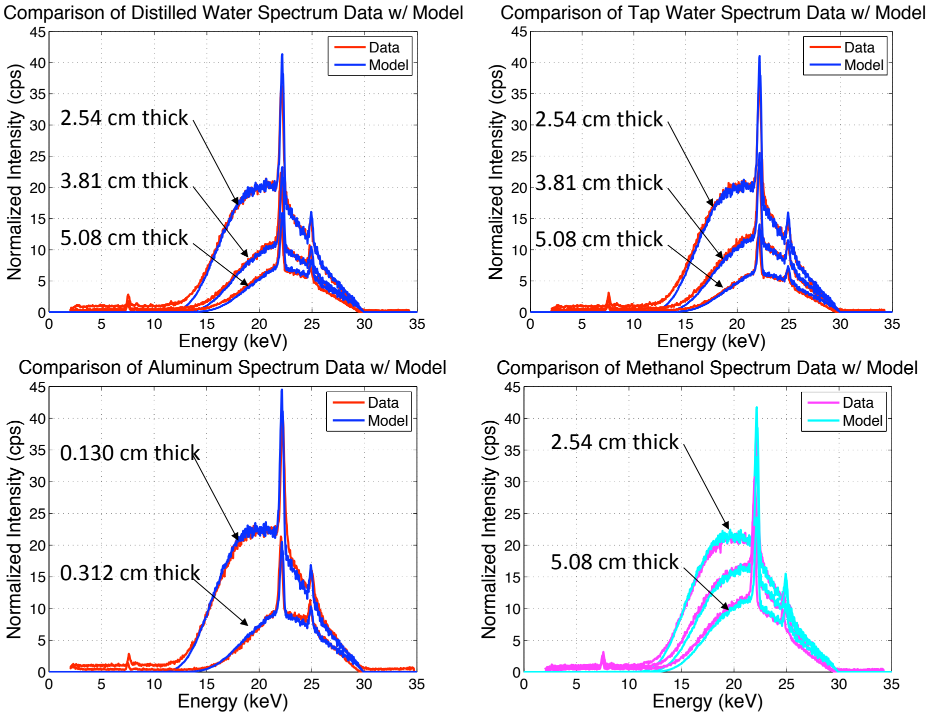

Figure 7.2: Comparison of forward spectral model obtained using Equation (2.1) (solid blue line) to experimental results taken with XR-100CR detector (solid red line) for samples of distilled water (top left), tap water (top right), aluminum (bottom left) and methanol (bottom right).

tenuation with the results of several measurements taken through samples of various mass thicknesses. Specifically, using the source spectrum shown in Figure 7.1, the attenuation of x-rays through samples of water, methanol and aluminum alloy 6061 of several different thicknesses were modeled using Equation (2.1) and compared with experimental measurements made using the procedure described in Section 5.1.1 and are shown in Figure 7.2. Excellent agreement can be found between the models and the experimental data, with the largest deviations occurring at low intensities where the signal falls below the noise floor of the experimental values due to limitations in the measurement system, which are not accounted for in the modeled results.

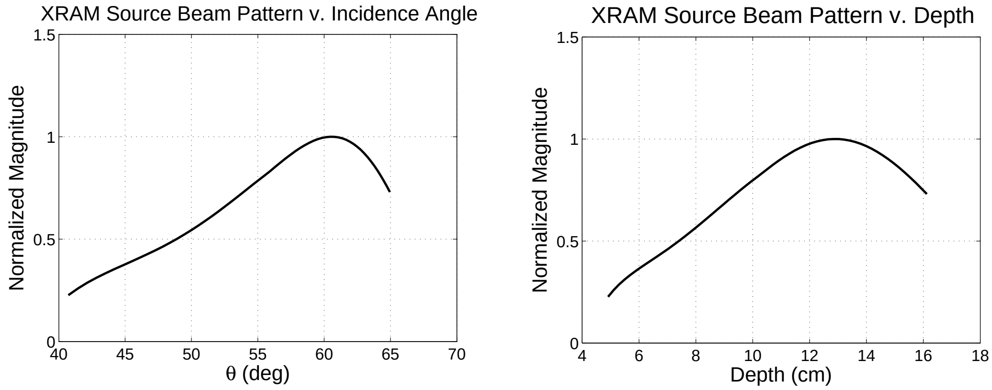

Figure 7.3: Normalized Eclipse II source beam pattern versus incidence angle (left) and detector depth (right), obtained from a 4th-order least-squares fit of water and methanol experimental data using Equation (4.28).

The observed spatial beam pattern of the Eclipse II source beam pattern is shown in Figure 7.3, and were obtained using Equation (4.28) and the method outlined in Section 6.2.2 using XRAM output from water and methanol samples. These results are illustrated in two different ways: as a function of depth and a function of incidence angle measured from the axis of the source. Although these two variables are related to one another according to Equation (4.12), each graph is useful in providing a full picture of the effect of the beam pattern. Specifically, the beam pattern plotted as a function of angle is useful in understanding this behavior relative to the source, and is a common method of characterizing the beam pattern of an acoustical source. However, in relation to the effect on the measurements made by the XRAM device, it is much more useful to look at the variation with respect to the depth of the detector.

Attenuation measurements were obtained using the procedure described in Section 5.2, and typical results are shown in Figure 7.4 in solid lines. These results are compared with the results of the XRAM integral model given by Equation (4.17), using the source spectrum given in Figure 7.1 and source beam pattern as a function of depth shown in the right panel of Figure 7.3 to obtain the modeled data for the liquid samples shown in the top panels of Figure 7.4 in dashed lines. The data points with error bars represent uncertainty for a 95% confidence interval determined using Equation (4.55), using the statistical differences between repeated

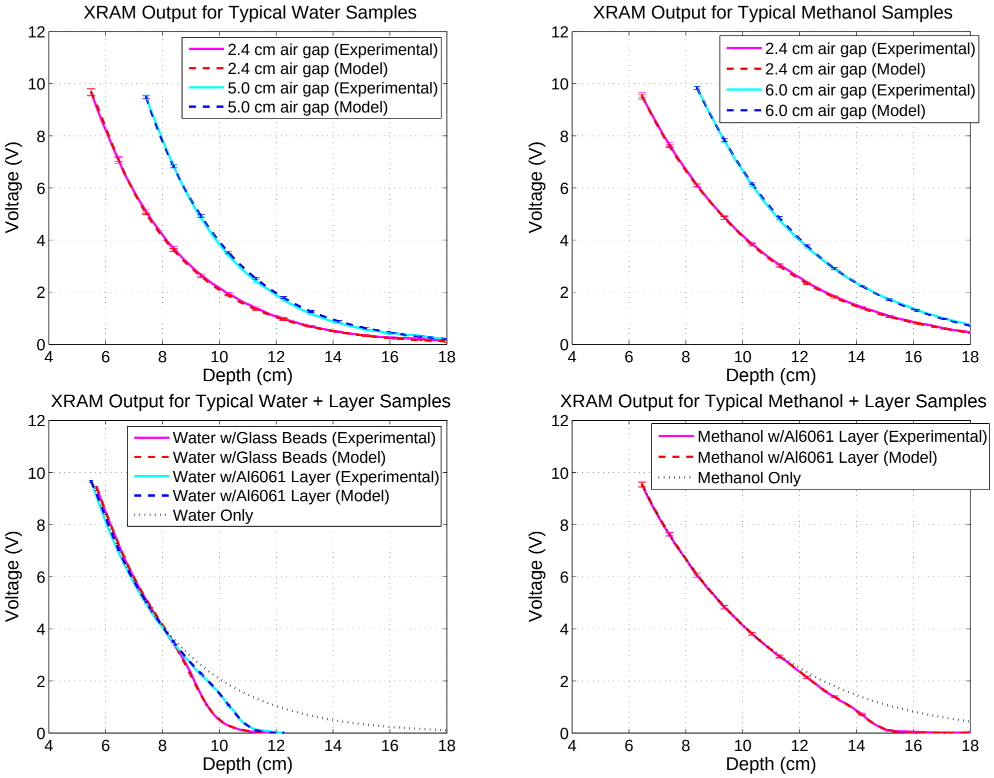

Figure 7.4: Comparison of experimental and modeled output voltage versus detector depth for a typical sample of water (top left), methanol (top right), water mixtures (bottom left) and methanol mixtures (bottom right).

measurements for the experimental results, and the differences between the modeled and measured output for the modeled results. Since the uncertainty varies slowly with depth, it is only shown every 1 cm for clarity. From the figures it can be seen that the model is in excellent agreement with the experimental data and accurately accounts for the changes in slope as a function of detector depth.

For the modeling of a single material sample, such as the cases involving only a liquid sample, knowing the air/sample interface depth and material properties (density and mass attenuation coefficient) is sufficient for modeling the XRAM output shown in the dashed lines in the top panels of Figure 7.4. When the sample contains two materials, such as the cases involving mixtures shown in the bottom panels of Figure 7.4, the measured results are used to determine the relative

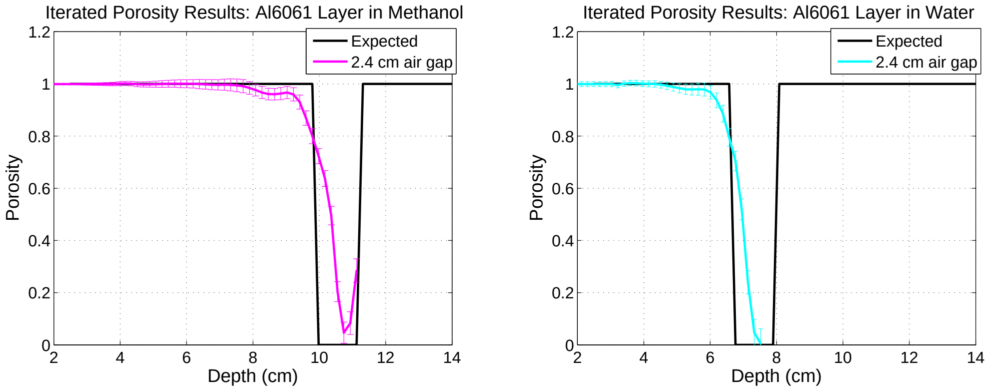

Figure 7.5: Inverted porosity using the Tikhonov regularization technique for a 1.34 cm thick 6061 aluminum alloy layer in methanol (left) and water (right) v. depth in sample.

amounts of each component (given by the porosity) as a function of depth. Using the Newton-Raphson iteration given by Equations (4.39) through (4.42) and the Tikhonov matrix regularization technique described in Section 4.4, the modeled data can be iterated until it is within a small finite range of the measured data. The final iteration of the modeled data is shown in dashed lines in the bottom panels of Figure 7.4, and lies on top of the measured data.

The porosity values obtained as a function of depth at this final iteration point are shown for liquids with an aluminum alloy layer in Figure 7.5 and water-saturated glass beads in Figure 7.6 over the depth range where a converged solution was obtained. The data points with error bars represent the uncertainty for a 95% confidence interval, determined using Equation (4.55). As a point of reference, a representation of the expected porosity for each case based on geometric measurements of the difference interface depths is shown in black.

Although the abrupt change in expected porosity at the interfaces may be somewhat idealized in the case of the water-saturated glass beads by not accounting for local variations in the sediment roughness, the aluminum alloy layer data in Figure 7.5 should be an accurate representation of the interface of water and aluminum, illustrating the limit in how steep of a change in porosity can be resolved. Except for the immediate area around the rapid change at the interface, the converged porosity values show good agreement with the expected porosity values

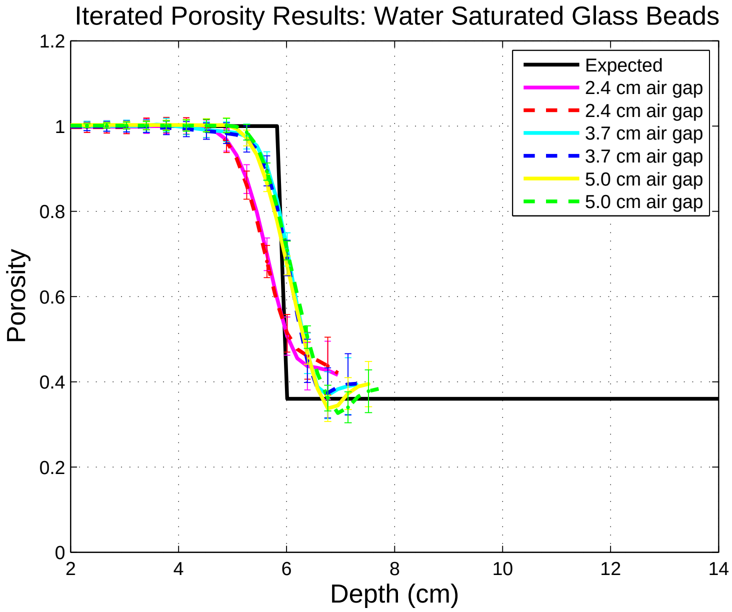

Figure 7.6: Inverted porosity using the Tikhonov regularization technique for water-saturated glass beads with three different thickness air gaps v. depth in sample.

for the liquid only and for the aluminum alloy. Although the exact porosity of the water-saturated sediment was not known, the porosity values obtained are within the range of accepted values for unconsolidated monodisperse glass beads [4].

Chapter 8

Conclusions

As described in Chapter 1, the objective of the X-Ray Attenuation Measurement (XRAM) system is to be a portable diver operated device that can perform direct *in situ* measurements of sediment density gradients without significant disruption of the test site. Based on the good agreement between experimental and predicted values for samples of different densities and density gradients described in Chapter 7, and the device's compact design and diver operated control systems discussed in Chapter 3, this objective has been achieved. Such measurements cannot be accomplished with existing techniques, hence this device may represent a significant step forward.

Although the current design meets these objectives, future versions of the XRAM device could be modified to increase the system performance. First, the depth range into the sediment of useful data could be improved by using a higher energy cold cathode x-ray source. Although the Eclipse II source represented the best source available at the time of construction, newer versions are now available that produce up to 45 keV. By increasing the energy the benefits are twofold; the linear attenuation coefficient decreases exponentially as a function of energy allowing x-rays to penetrate deeper into the sample, and these higher energy x-rays occur in the Compton region which is largely independent of atomic mass and vary much less with energy, so that the behavior of x-ray interactions is dominated by the density.

Second, additional improvements in the quality of data obtained at a given depth could be achieved by reconfiguring the location of the source so that it transmits across the layer of interest. In the current design, the measured data at a given depth included the layer of interest plus all the previous layers. This decreased the sensitivity of the system with increasing depth, and made it necessary to use matrix regularization to determine the density gradient, both of which limited the precision of the density gradient measurements. By transmitting only across the layer of interest, say by keeping the detector and source parallel and lowering them together, higher quality data can be obtained at a given sample layer. This can be further improved by using a narrow beam source, which would reduce the effect of scattered x-ray energy at the detector and eliminating the need for a buildup factor.

Finally, the capabilities of the current version of the XRAM device could be significantly expanded by use of a spectrum analyzer detector for obtaining *in situ* data, similar to the system used to determine the source spectrum. By looking at the spectrum after passing through a stratified sediment sample, information on the specific composition of each layer could be determined based on the energy at which x-ray characteristics in the measured spectrum occur, and the corresponding amplitude.

Bibliography

[1] R. J. Urick, *Principles of Underwater Sound.* New York: McGraw-Hill, 1983.

[2] G. V. Frisk, *Ocean and Seabed Acoustics.* Englewood Cliffs, NJ: P T R Prentice Hall, 1994.

[3] M. Kimura and T. Tsurumi, "Characteristics of acoustic wave reflections from the transition layer of surficial marine sediment," *IEEE Proceedings of the 2002 Int'l Symposium on Underwater Technology*, pp. 225–230, 2002.

[4] D. R. Jackson and M. D. Richardson, *High-Frequency Seafloor Acoustics.* New York: Springer, 2007.

[5] D. Tang, K. B. Briggs, K. L. Williams, D. R. Jackson, E. I. Thorsos, and D. B. Percival, "Fine-scale volume heterogeneity measurements in sand," *IEEE Journal of Oceanic Engineering*, **27**, pp. 546–560, July 2002.

[6] T. H. Orsi and A. L. Anderson, "Bulk density calibration for x-ray tomographic analyses of marine sediments," *Geo-Marine Letters*, **19**, pp. 270–274, December 1999.

[7] M. D. Richardson and K. B. Briggs, "In situ laboratory geoacoustic measurements in soft mud and hard-packed sand sediments: Implications for high-frequency acoustic propagation and scattering," *Geo-Marine Letters*, **16**, pp. 196–203, September 1996.

[8] "Sediment acoustics experiment 2004 (SAX04) images," *http://www.apl.washington.edu/projects/SAX04/images.html* [Last viewed on: 8/12/2009].

[9] G. F. Knoll, *Radiation Detection and Measurement.* New York: John Wiley & Sons, 1989.

[10] J. H. Hubbell and S. M. Seltzer, "Tables of x-ray mass attenuation coefficients and mass energy-absorption coefficients (version 1.4)."

[11] J. K. Shultis and R. E. Faw, *Radiation Shielding.* La Grange Park, IL: American Nuclear Society, Inc., 2000.

[12] J. Stewart, *Calculus Concepts and Contexts.* Pacific Grove, CA: Brooks/Cole Publishing Company, 1998.

[13] R. S. Figliola and D. E. Beasley, *Theory and Design for Mechanical Measurements.* New York: John Wiley & Sons, 2000.

[14] R. Penrose, "A generalized inverse for matrices," *Proceedings of the Cambridge Philosophical Society*, **51**, pp. 406–413, 1955.

[15] A. Neumaier, "Solving ill-conditioned and singular linear systems: A tutorial on regularization," *SIAM Review*, **40**, pp. 636–666, September 1998.

[16] A. N. Tikhonov, "Solution of incorrectly formulated problems and the regularization method," *Soviet Mathematics Doklady*, **4**, pp. 1035–1038, 1963.

[17] S. F. Wagner, *Introduction to Statistics.* New York: Harper Collins, 1991.

[18] M. Abramowitz and I. A. Stegun, eds., *Handbook of Mathematical Functions with Formulas, Graphs and Mathematical Tables.* New York: Dover, 1972.

[19] "XR-100CR x-ray detector," January 2009, *http://www.amptek.com/xr100cr.html* [Last viewed on: 8/12/2009].

[20] "Alcoa engineered products: Understanding extruded aluminum alloys," January 2002, *http://www.alcoa.com/adip/catalog/pdf/Extruded_Alloy_60056105.pdf* [Last viewed on: 8/12/2009].

Vita

Matthew David Guild was born in Stoneham, Massachusetts on March 13, 1982, the son of Johnette Marie Guild and Richard Leonard Guild. After finishing high school at Austin Preparatory School, Reading, Massachusetts, in 2000, he entered Boston University in Boston, Massachusetts, as a Cardinal Medeiros Scholarship recipient. In May 2004, he graduated *summa cum laude* with a Bachelor of Science in Aerospace Engineering from Boston University. Since June 2004, Matthew has been working at the Applied Research Laboratories, University of Texas at Austin (ARL:UT), and has been enrolled at the University of Texas at Austin since August 2004.

Permanent Address: 9009 Great Hills Trail
Apt. 1032
Austin, TX 78759

This thesis was typeset with LaTeX 2ε[1] by the author.

---

[1] LaTeX 2ε is an extension of LaTeX. LaTeX is a collection of macros for TeX. TeX is a trademark of the American Mathematical Society. The macros used in formatting this thesis were written by Dinesh Das, Department of Computer Sciences, The University of Texas at Austin, and extended by Bert Kay, James A. Bednar, and Ayman El-Khashab.